

Shape optimization approach to defect-shape identification with convective boundary condition via partial boundary measurement

Julius Fergy T. Rabago · Hideyuki Azegami

Received: date / Accepted: date

Abstract We aim to identify the geometry (i.e., the shape and location) of a cavity inside an object through the concept of thermal imaging. More precisely, we present an identification procedure to determine the geometric shape of a cavity with convective boundary condition in a heat-conducting medium using the measured temperature on a part of the surface of the object. The inverse problem of identifying the cavity is resolved by shape optimization techniques, specifically by minimizing a least-squares type cost functional over a set of admissible geometries. The computation of the first-order shape derivative or shape gradient of the cost is carried out through minimax formulation, which is then justified by the Correa-Seeger theorem coupled with function space parametrization technique. We further characterize its boundary integral form using some identities from tangential calculus. Then, we utilize the computed expression for the shape gradient to implement an effective boundary variation algorithm for the numerical resolution of the shape optimization problem. To avoid boundary oscillations or irregular shapes in our approximations, we execute the gradient-based scheme using the H^1 gradient method with perimeter regularization. Also, we propose a novel application of the said method in computing the mean curvature of the free boundary appearing in the shape gradient of the cost functional. We illustrate the feasibility of the proposed method by testing the numerical scheme to several cavity identification problems. Additionally, we also give some numerical examples for the case of corrosion detection since its inverse problem interpreted in the framework of electrostatic imaging is closely related to the focused problem.

Keywords Shape identification · shape optimization · geometric inverse problem · Lagrange multiplier method · minimax formulation

J. F. T. Rabago
Graduate School of Informatics, Nagoya University
A4-2 (780) Furo-cho, Chikusa-ku, Nagoya 464-8601, Japan
E-mail: jfrabago@gmail.com

H. Azegami
Graduate School of Informatics, Nagoya University
A4-2 (780) Furo-cho, Chikusa-ku, Nagoya 464-8601, Japan

1 Introduction

In this work we are primarily concern with a nonlinear inverse-geometry heat transfer problem where the shape solution is found based on the temperature measured on a part of the boundary of the object. Our particular interest is the identification of the shape and location of a defect with convective boundary condition.

1.1 Background of the Study

The means of recovering the shape of a defect, i.e., a cavity, corrosion, etc., using internal thermal properties of an object is called thermal imaging (the static temperature and heat flow are measured). Such a procedure is popular in the fields of civil and mechanical engineering, and is widely employed in non-destructive testing and evaluation. It has the additional advantage of allowing defect inspection via existing surfaces [38]. Under this setup, the specimen is heated on a part of its surface becoming an assigned temperature and the resulting temperature response on the remaining part is observed. Such arrangement for an identification task corresponds to a partially overdetermined boundary data (whereas a complete use of the specimen's surface for inspection or measurement results to a complete overdetermined boundary data). Another process of detecting defects that is closely related to thermal imaging is called electrostatic imaging. In this case, the static voltage and surface current measurements are used to determine the conductivity distribution in the interior of the specimen (see, e.g., [41]). This technique is usually applied to corrosion detection problems. Both methods are widely used in engineering sciences, and have already gained considerable interests from many mathematicians and researchers working in the area of geometric inverse problems. As we have witnessed, these problems still continue to attract attentions of scientists and researchers as they remain challenging both in terms of their mathematical and numerical aspects.

Quite recently, concerning the theoretical aspect of a related problem, Bacchelli [11] studied the problem of determining the corroded portion of the boundary of an n -dimensional body ($n = 2, 3$) and the impedance by two measures on the accessible portion of the boundary. In her study, a Robin homogeneous condition was assumed on the unknown boundary part. Meanwhile, Pagani and Pierotti [44] studied the inverse problem of recovering the shape of a cavity or of a crack contained in a connected domain Ω , and the problem of reconstructing part of the boundary $\partial\Omega$ itself, when a condition of the third kind or Robin condition is prescribed on the defects. These authors proved a result of *uniqueness* by two measures.

In terms of experimental and numerical treatment of the problem, we have a very recent work of Kurahashi et al. [38] on three-dimensional shape identification of defects in a structure using the temperature history on the specimen's surface. The authors applied a finite element method to simulate the temperature distribution in the test piece, and the adjoint variable method was employed to identify the cavity's shape. On the other hand, in [36], Kazemzadeh-Parsi and Daneshmand presented a system identification scheme to determine the geometric shape of a cavity with convective boundary condition, again, under the context of thermal imaging. In their work, the authors proposed a new approach based on non-boundary-fitted meshes and gradient smoothing technique to deal with the direct problem and shape sensitivity analysis. Afterwards, the authors used a conjugate gradient method for the optimization algorithm. The new approach, called as *smoothed fixed-grid finite-element method* or *SFGFEM*, used in [36] was actually used only for the solution of the forward problem. The main objective of the SFGFEM is to improve the accuracy of the

formulation of the boundary-intersecting elements. In the said method, the homogenization technique is disregarded and the element matrices for the boundary-intersecting elements are expressed as domain integrals over the internal parts of these elements. The gradient smoothing technique is then used to evaluate these integrals numerically via transferring them to the line integration (see [36] for further details).

In this study, we shall use shape optimization techniques to solve a geometric inverse problem inspired by the two above-mentioned investigations, thereby providing an alternative computational strategy in solving the inverse problem. Additionally, in the course of resolving the inverse problem, we shall demonstrate how the primary information used in the inversion procedure can be exploited to obtain the best result for the inversion process.

1.2 The Mathematical Model

In Kurahashi et al.'s work on shape identification of defects [38], the mathematical model is formulated in the following fashion. The whole domain of the material or test piece with a cavity is denoted by $\Omega \subset \mathbb{R}^3$. Its boundary $\partial\Omega$ consists of the outside boundary Γ and the boundary of the cavity Γ_C . Furthermore, Γ consists of the heated boundary Γ_P with a prescribed temperature and the measurement boundary Γ_M . The temperature distribution, which we denote here by u , was assumed to satisfy the heat transfer equation $\rho c \partial_t u - k \Delta u = 0$ having the following initial and boundary conditions:

$$\begin{cases} u = u_0 & \text{in } \Omega, \\ u = u_P & \text{on } \Gamma_P, \\ -k \partial_{\mathbf{n}} u = h_M(u - u_\infty) & \text{on } \Gamma_M, \\ -k \partial_{\mathbf{n}} u = h_C(u - u_C) & \text{on } \Gamma_C. \end{cases} \quad (1)$$

The constants ρ , c , k , h_M , h_C , u_∞ , u_C and u_P denote the density, specific heat, thermal conductivity, the convective heat transfer coefficient of the outside boundary, the convective heat transfer coefficient of the space inside the cavity, the ambient temperature, the temperature inside the cavity and the prescribed temperature on the heated boundary Γ_P , respectively. Moreover, \mathbf{n} represents the normal outward direction to the boundary and $\partial_{\mathbf{n}} u := \nabla u \cdot \mathbf{n}$ denotes the normal derivative of u .

In this study, we shall instead consider a general steady-state heat transfer problem defined on a two-dimensional connected bounded domain Ω . Similar to [38], its boundary $\partial\Omega$ consists of two disjoint components; the outer boundary Γ , which is accessible for inspection or measurements, and the boundary of an inner cavity Γ_C . The boundary Γ is divided into two parts, namely, Γ_M and Γ_P . Moreover, \mathbf{n} represents the normal outward direction to the boundary. The boundaries Γ_P , Γ_M and Γ_C , respectively, denote the heated surface (or boundary in the two-dimensional case), the outside surface where measurement is performed and the surface of the cavity. Here we adopt the set of boundary conditions given in [38], specifically taking into account the assumptions made by the authors on Γ_C . We emphasize that the convective boundary condition on Γ_C was in fact due to the influence of the convective heat transfer from the air within the cavity. This indication was based on the observation made by Kurahashi et al. [38] on the experiment they conducted using the non-destructive thermal testing method. In addition, we also include prescribed heat fluxes on the boundaries Γ_M and Γ_C to cover a similar mathematical formulation considered in [36]. As a result, the

governing equation and the boundary conditions are given as follows:

$$\begin{cases} -k\Delta u = 0 & \text{in } \Omega, \\ u = u_P & \text{on } \Gamma_P, \\ -k\partial_{\mathbf{n}}u = h_M(u - u_\infty) - Q_M & \text{on } \Gamma_M, \\ -k\partial_{\mathbf{n}}u = h_C(u - u_C) - Q_C & \text{on } \Gamma_C. \end{cases} \quad (2)$$

The definitions of the constants are the same as before, but, in addition, Q_M and Q_C are the respective prescribed heat fluxes on Γ_M and Γ_C . At this juncture, it is worth mentioning that the governing equation for the case of corrosion detection problem can be obtained by slightly modifying equation (2). In the literature, such problem is modelled by supposing that a Laplace's equation holds in the interior of the specimen and the effect of corrosion is described by means of a boundary condition of the Robin condition. More precisely, the detection problem may be stated as follows. We assume a bounded connected planar domain Ω whose boundary $\partial\Omega$ is composed of two open disjoint parts, one of which is available for observation (i.e., accessible for input and output measurements) and the other one is inaccessible and in fact is unknown *a priori*. Then, by denoting the known portion by Γ and the remaining part by $\Gamma_C = \partial\Omega \setminus \bar{\Gamma}$, one describes the corresponding system of partial differential equation (PDE) for the corrosion detection problem as follows:

$$-\Delta u_D = 0 \text{ in } \Omega, \quad u_D = f \text{ on } \Gamma, \quad \partial_{\mathbf{n}}u_D + \lambda u_D = 0 \text{ on } \Gamma_C, \quad (3)$$

where \mathbf{n} is the exterior unit normal to Γ_C , $f \neq 0$ is an assigned function, and $\lambda \geq 0$ is a fixed number. In (3), we put the subscript D in the variable u to emphasize that we are prescribed with the Dirichlet data f on the accessible boundary Γ . In contrast, the variable u_N will be introduced in later discussion. Such problem has been examined, for instance, in [29]. The study of such a model stems from a number of indications. A first indication is based on the observation that corrosion tends to roughen a surface, which can be modeled by the introduction of a thin coating characterized by rapid oscillations. In the limit where the thickness of the coating goes to zero and the rapidity of the oscillations diverges, a Robin condition has been derived as was shown in [16]. Meanwhile, in the context of electrochemical corrosion processes, the study can be based on Faraday's law which says that the mass loss is proportional to the normal current flux (see, e.g., [32, Section 3.1]). In [50], a potential model of this kind of process is proposed, and as pointed out in [28], linearizing with respect to the transfer coefficient, the nonlinear boundary conditions in [50] will eventually lead to a Robin condition.

1.3 Shape Optimization Formulation

In the formulation of forward (or direct) problems, the geometric profile of the domain is assumed to be known; i.e., the shape and the location of the defect are specified. Clearly, in this situation, the mathematical problem is well-posed and the temperature distribution over the entire solution domain can easily be determined. Conversely, in the case of inverse-geometry problems, the shape and the location of the cavity is unknown *a priori* and must be fully resolved using extra temperature measurements on a part of the outer boundary. Such an additional information allows us to conduct inverse analyses for the given inverse problem.

In reference to problem (2), the additional temperature measurement, which we denote here by u_M , on the boundary Γ_M will result to an overdetermined boundary condition of Γ_M , and therefore making it an ill-posed problem. The solution to the PDE system (2) with the additional boundary condition $u = u_M$ on Γ_M can be found by employing the methods of shape optimization (see, e.g., the books [22, 48]). This can be done by either tracking the Dirichlet or Neumann data in a least-squares sense relative to $L^2(\Gamma_M)$. In our case, since we are prescribed with the Robin condition on Γ_M , we shall track the Dirichlet data in a least-squares sense relative to $L^2(\Gamma_M)$ and consider the minimization problem

$$\min_{\Gamma_C \in \mathcal{O}_{\text{ad}}} \left\{ \mathcal{J}(\Gamma_C) := \frac{1}{2} \int_{\Gamma_M} (u - u_M)^2 ds \right\}, \quad (4)$$

where \mathcal{O}_{ad} is some admissible set of geometries and the state variable $u := u(\Omega)$ satisfies the mixed boundary value problem (BVP) (2). In this work, we shall consider $C^{k,1}$ -domains, $k \geq 1$. Particularly, in the case of cavity identification problem, we assume that Ω has $C^{1,1}$ regularity in order to establish the shape derivative of the cost functional $\mathcal{J}(\Gamma_C)$.

In the case of corrosion detection problem, if, for instance, Ω is a $C^{k,1}$ domain, we may let $g \in H^{k-1/2}(\Gamma)$ be an admissible boundary measurement for the Neumann data, i.e., g belongs to the image of the Dirichlet-to-Neumann operator defined by $\Lambda_\Gamma : u|_\Gamma \in H^{k+1/2}(\Gamma) \mapsto \partial_n u \in H^{k-1/2}(\Gamma)$, where u is the unique solution of (2). The additional boundary condition $\partial_n u = g$ on Γ_C again results to an overdetermined boundary problem, which, as we have mentioned, can be treated by shape optimization techniques. In this situation, one may opt to track the Neumann data in the $L^2(\Gamma)$ least-squares sense and consider the optimization problem

$$\min_{\Gamma_C \in \tilde{\mathcal{O}}_{\text{ad}}} \left\{ \mathcal{J}_N(\Gamma_C) := \frac{1}{2} \int_{\Gamma} (\partial_n u_D - g)^2 ds \right\}, \quad (5)$$

where $\tilde{\mathcal{O}}_{\text{ad}}$ denotes some admissible set of geometries. However, such option for the cost functional requires more regularity of the state variable u to be well defined. For instance, an H^3 -regularity ($k = 2$) of the state u is sufficient to obtain the shape derivative of \mathcal{J}_N with respect to Ω . As a consequence, it may be impractical to use this functional in numerical experiments where higher regularity of the state variables is not guaranteed.

Shape optimization strategies have already been applied in resolving geometric inverse problems, particularly in identifying cavities in linear elasticity [13, 30, 31, 39] and thermoelasticity [14], as well as in recovering an inclusion through the notion of electrostatic imaging [1]. In [13] and [14], the inverse problem in linear elasticity was examined using a complete overdetermined boundary data, while in [1, 30, 31] and [39], the overdetermined condition only appears on a part of the boundary. Recently, a related problem concerning a shape optimization approach for the inverse obstacle problem with generalized impedance boundary conditions was investigated in [19]. In the aforementioned study, however, a complete boundary measurement was used for solving the inverse problem and, in addition, a Neumann-tracking type cost functional was utilized in realizing the shape identification procedure. Furthermore, a closely similar problem, but nevertheless the same, was also examined in [49]. The author consider a boundary detection problem inspired by the notion of electrostatic imaging. The mathematical model involves a boundary condition of the third kind on a part of the accessible and unknown boundary of the planar domain, and the geometry of the inaccessible boundary was determined using the Cauchy data on the other part of the accessible boundary. Also, a Neumann-tracking type cost functional was used to examine the inverse problem wherein the main purpose of the study is to address the question of existence of solution for the given shape optimization problem. We mentioned that there are

other known approaches in resolving inverse problems. One approach that is based on the method of fundamental solutions was used in [33,34] to solve an inverse problem in linear elasticity setting.

Noting in mind the above-mentioned works, and to the best of our knowledge, this present work is the first to examine a geometric inverse problem with partial boundary measurement consisting of a convective boundary condition on the unknown boundary under the framework of shape optimization with a Dirichlet-tracking type cost functional. We stress that the present formulation and methodology in treating the given inverse problem closely mimics actual experimental procedure such as that seen in [38]. These facts further warrant the necessity to accomplish the present investigation. In this work, we shall focus our attention to the computation of the first-order shape derivative or shape gradient of the cost functional $\mathcal{J}(\Gamma_C)$ since our ultimate goal is to carry out a shape optimization approach for the cavity identification problem. Nevertheless, the shape derivative of the cost functional $\mathcal{J}_N(\Gamma_C)$, as well as the shape derivative of the corresponding cost functional for tracking the Dirichlet data for the corrosion detection problem, can easily be established following the same line of arguments in exhibiting the case for the focused problem.

The rest of the paper is structured as follows. In Section 2, we briefly discuss the requisites of our present investigation. The minimax formulation and formal computation of the shape gradient is presented in Section 3. Then, in Section 4, we give details on an iterative solution procedure based on the so-called H^1 gradient method. A variety of numerical studies are then discussed in Section 5. Lastly, in Section 6 a conclusion is stated and topics for future investigation are offered.

2 Preliminaries

In this section we provide the requisites of our investigation. First, we briefly discuss the variational form of the state problem. Then, we give a short discussion of the velocity method from shape optimization which can be used to compute the shape derivative of the functional $\mathcal{J}(\Gamma_C)$. We end the section by giving out some useful identities from tangential calculus. The formal analysis of these topics are delivered, for instance, in [22,48].

2.1 Variational Form of the State Problem

In this work, we consider the Hilbert space

$$W(\Omega) = \{\varphi \in H^1(\Omega) : \varphi|_{\Gamma_P} = 0\},$$

endowed with the norm

$$\|\varphi\|_{W(\Omega)}^2 := \|\nabla\varphi\|_{L^2(\Omega)}^2 + \|\varphi\|_{L^2(\Gamma_M)}^2 + \|\varphi\|_{L^2(\Gamma_C)}^2, \quad (6)$$

and a linear manifold defined by

$$W_v(\Omega) = \{\varphi \in H^1(\Omega) : \varphi|_{\Gamma_P} = v\},$$

for $v \in H^{\frac{1}{2}}(\Gamma_P)$.

Given the above definition, the variational formulation of (2) is given as follows: find $u \in H^1(\Omega)$ such that

$$\int_{\Omega} k \nabla u \cdot \nabla \varphi \, dx + \int_{\Gamma_M} \{h_M(u - u_{\infty}) - Q_M\} \varphi \, ds + \int_{\Gamma_C} \{h_C(u - u_C) - Q_C\} \varphi \, ds = 0, \quad (7)$$

for all $\varphi \in W(\Omega)$, and $u = u_P$ on Γ_P . Equation (7) can be shown to have a unique solution through Lax-Migram lemma.

2.2 The Velocity (or Speed) Method

Let \mathbf{V} be an element of $C([0, \varepsilon]; \mathcal{D}^k(\mathbb{R}^2, \mathbb{R}^2))$, for some integer $k \geq 2$ and a small real number $\varepsilon > 0$, where $\mathcal{D}^k(\mathbb{R}^2, \mathbb{R}^2)$ denotes the space of k -times continuously differentiable functions with compact support contained in \mathbb{R}^2 . The field $\mathbf{V}(t)(x) = \mathbf{V}(t, x)$, $x \in \mathbb{R}^2$, is an element of $\mathcal{D}^k(\mathbb{R}^2, \mathbb{R}^2)$ which may depend on $t \geq 0$. It generates the transformations $T_t(\mathbf{V})(X) := T_t(X) = x(t; X)$, $t \geq 0$, $X \in \mathbb{R}^2$, through the differential equation

$$\frac{d}{dt} x(t; X) = \mathbf{V}(t, x(t; X)), \quad x(0; X) = X,$$

with the initial value X given. We denote the ‘transformed domain’ $T_t(\mathbf{V})(\Omega)$ at $t \geq 0$ by $\Omega_t(\mathbf{V})$, or simply $\Omega_t =: T_t(\Omega)$. In the case of (single) cavity identification problem, the domain $\Omega = \Omega_0$ in consideration is of annular type with boundary $\partial\Omega$ which is the union of two disjoint sets: the known (accessible) boundary $\Gamma := \Gamma_M \cup \Gamma_P$ and the unknown (inaccessible) boundary Γ_C . In this work, the evolutions of the domain Ω are described using time-independent velocity fields

$$\mathbf{V} \in \Theta_k := \{\mathbf{V} \in (C^{k,1}(\overline{\Omega}), \mathbb{R}^2) : \mathbf{V}|_{\Gamma} = 0\}. \quad (8)$$

In above definition, every admissible deformation field \mathbf{V} forces Γ to remain invariant. For $t \in [0, \varepsilon]$, where ε is some sufficiently small number, one can show, following the line of arguments in [9, Lemma 11], that T_t is invertible, and that $T_t, T_t^{-1} \in \mathcal{D}^1(\mathbb{R}^2, \mathbb{R}^2)$. Furthermore, the quantity $I_t := \det DT_t(X)$ is strictly positive, where $DT_t(X)$ is the Jacobian matrix of the transformation $T_t = T_t(\mathbf{V})$ associated with the velocity field \mathbf{V} . In this paper, for simplicity, we write $A_t = I_t(DT_t^{-1})(DT_t)^{-T}$ and $w_t = I_t|(DT_t)^{-T}\mathbf{n}|$ (referred to as the Jacobian matrix of T_t with respect to the boundary $\partial\Omega$), where $(DT_t)^{-1}$ and $(DT_t)^{-T}$ denote the inverse and inverse transpose of the the Jacobian matrix DT_t , respectively.

2.3 Some Useful Lemmas

The following lemmas will be essential to our analysis.

Lemma 1 *Let $\varphi_t \in L^1(\Omega_t)$ and $\psi_t \in L^1(\partial\Omega_t)$, then $\varphi_t \circ T_t \in L^1(\Omega)$ and $\psi_t \circ T_t \in L^1(\partial\Omega)$, respectively. Moreover, the following domain and boundary transformations hold:*

$$\int_{\Omega_t} \varphi_t \, dx_t = \int_{\Omega} \varphi_t \circ T_t I_t \, dx, \quad \int_{\partial\Omega_t} \psi_t \, ds_t = \int_{\partial\Omega} \psi_t \circ T_t w_t \, ds.$$

Lemma 2 *Let Ω be a $C^{1,1}$ -domain with boundary $\partial\Omega = \Gamma \cup \Gamma_C$ and $\mathbf{V} \in \Theta_1$. For $\varphi, \psi \in H^2(\Omega)$, we have*

$$\begin{aligned} \int_{\Omega} k A'_0 \nabla \varphi \cdot \nabla \psi \, dx &= \int_{\Omega} k \Delta \varphi (\mathbf{V} \cdot \nabla \psi) \, dx + \int_{\Omega} k \Delta \psi (\mathbf{V} \cdot \nabla \varphi) \, dx + \int_{\Gamma_C} k (\nabla \varphi \cdot \nabla \psi) \mathbf{V} \cdot \mathbf{n} \, ds \\ &\quad - \int_{\Gamma_C} k \partial_{\mathbf{n}} \varphi (\mathbf{V} \cdot \nabla \psi) \, ds - \int_{\Gamma_C} k \partial_{\mathbf{n}} \psi (\mathbf{V} \cdot \nabla \varphi) \, ds, \end{aligned}$$

where $A'_0 = \operatorname{div} \mathbf{V} \mathbf{I}_2 - D\mathbf{V} - (D\mathbf{V})^T$ and \mathbf{I}_2 denotes the second-order identity matrix.

Proof The identity can be confirmed without any difficulty following the proof of [9, Lemma 32]. Alternatively, we may proceed briefly as follows. Since $\varphi, \psi \in H^2(\Omega)$, we have $\nabla^2 \varphi, \nabla^2 \psi \in L^2(\Omega)$, $\Delta \varphi, \Delta \psi \in L^2(\Omega)$, and we infer that $\nabla \varphi \cdot \nabla \psi \in W^{1,1}(\Omega)$. Moreover, we have the classical identity (see, e.g., [1, Eq. (3.10)])

$$\nabla \varphi \cdot A'_0 \nabla \psi = (\nabla \varphi \cdot \mathbf{V}) \Delta \psi + (\nabla \psi \cdot \mathbf{V}) \Delta \varphi - \operatorname{div} B,$$

where $B = (\nabla \varphi \cdot \mathbf{V}) \nabla \psi + (\nabla \psi \cdot \mathbf{V}) \nabla \varphi - (\nabla \varphi \cdot \nabla \psi) \mathbf{V}$. Then, the desired result easily follows from the application of the divergence theorem (which is allowed since Ω is a bounded $C^{1,1}$ domain) together with the definition of elements of the set Θ_1 .

Here, we stress that we do not actually have the higher regularity $H^2(\Omega)$ for the unique solution u of the variational equation corresponding to our state problem (2). This lack of regularity is primarily due to the fact that the solution may be ‘singular’ around the transition points between Γ_P and Γ_M (see, e.g., [6] and the references therein), even if we have a $C^{1,1}$ regularity on the boundary $\partial\Omega$. We point out that we need an H^2 regularity for the state solution u (as well as an H^2 regularity for the adjoint solution p which we will describe later on) for us to be able to write the shape gradient of the cost in terms of just a boundary integral through the aid of Lemma 2. In this work, we will utilize the boundary expression for the shape gradient to formulate a boundary variation algorithm for the numerical realization of the minimization problem (4). We emphasize, however, that, away from the point of singularities, the solution to (2) in fact has the higher regularity H^2 . So, to get around the difficulty of having the desired regularity for the state solution, we can instead subtract off the singularities appearing at the points of transition between Γ_P and Γ_M from the solution of (2) and then consider the solution of a related Laplace equation which satisfies related boundary conditions, now having an H^2 regularity, as our new state solution. This remedy could be realized by combining the ideas issued in [12, 42, 51].

Finally, to end this section, we recall the so-called tangential Green’s formula (cf. [22, Eq. 5.27, p. 498]) which is a key identity in computing the boundary expression for the shape derivative of $\mathcal{J}(\Gamma_C)$.

Lemma 3 (Tangential Green’s formula) *Let U be a bounded domain of class $C^{1,1}$ and $\Omega \subset U$ with boundary Γ . Also, let $\mathbf{V} \in C^{1,1}(\overline{U}, \mathbb{R}^2)$ and $f \in W^{2,1}(U)$ be given, then*

$$\int_{\Gamma} (f \operatorname{div}_{\Gamma} \mathbf{V} + \nabla_{\Gamma} f \cdot \mathbf{V}) \, ds = \int_{\Gamma} \kappa f \mathbf{V} \cdot \mathbf{n} \, ds, \quad (9)$$

where κ is the mean curvature of Γ and the tangential gradient ∇_{Γ} is given by

$$\nabla_{\Gamma} f = \nabla f|_{\Gamma} - (\partial_{\mathbf{n}} f) \mathbf{n}.$$

3 Shape Gradient by Minimax Differentiability

In this section we shall demonstrate how the shape gradient of the cost functional can be established through a minimax of a suitable Lagrangian functional.

3.1 Minimax formulation

In the sequel, we present the minimax formulation of the cost functional $\mathcal{J}(\Gamma_C)$. To begin with, we define the functionals \mathcal{F} and \mathcal{L} as follows:

$$\begin{aligned}\mathcal{F}(\Omega, \varphi) &= \frac{1}{2} \int_{\Gamma_M} (\varphi - u_M)^2 ds, \\ \mathcal{L}(\Omega, \varphi, \psi) &= \int_{\Omega} k \nabla \varphi \cdot \nabla \psi dx + \int_{\Gamma_P} (\varphi - u_P) \mu ds + \int_{\Gamma_M} \{h_M(\varphi - u_\infty) - Q_M\} \psi ds \\ &\quad + \int_{\Gamma_C} \{h_C(\varphi - u_C) - Q_C\} \psi ds,\end{aligned}\quad (10)$$

where $\mu := \partial_{\mathbf{n}} \psi \in H^{\frac{1}{2}}(\Gamma_P)$ is a Lagrangian multiplier.

Next, we construct the functional $\mathcal{G}(\Omega, \varphi, \psi)$ as

$$\mathcal{G}(\Omega, \varphi, \psi) = \mathcal{F}(\Omega, \varphi) + \mathcal{L}(\Omega, \varphi, \psi),$$

where $\varphi \in H^1(\Omega)$ and $\psi \in W(\Omega)$. Given this definition, one can check that

$$\mathcal{J}(\Gamma_C) = \min_{\varphi \in H^1(\Omega)} \sup_{\psi \in W(\Omega)} \mathcal{G}(\Omega, \varphi, \psi)$$

since

$$\sup_{\psi \in W(\Omega)} \mathcal{G}(\Omega, \varphi, \psi) = \begin{cases} \mathcal{F}(\Omega, \varphi), & \text{if } \varphi = u, \\ +\infty, & \text{else.} \end{cases}$$

The Lagrangian \mathcal{G} is convex continuous with respect φ and is concave continuous with respect to ψ . Therefore, in accordance with the result issued in [24, Proposition 1.6, pp. 169-170] by Ekeland and Temam, the functional has a saddle point (u, p) if and only if (u, p) solves the following system of equations:

$$\mathcal{L}(\Omega, u, \varphi) = 0, \quad \forall \varphi \in W(\Omega), \quad (11)$$

$$d_{\varphi} \mathcal{F}(\Omega, u; \varphi) + d_{\varphi} \mathcal{L}(\Omega, u, p; \varphi) = 0, \quad \forall \varphi \in W(\Omega). \quad (12)$$

The first equation is actually equivalent to the state problem (2), hence the notation u . Meanwhile, the second one can easily be shown to be equivalent to the adjoint state system

$$\begin{cases} -k \Delta p = 0 & \text{in } \Omega, \\ p = 0 & \text{on } \Gamma_P, \\ -k \partial_{\mathbf{n}} p = h_M p + u - u_M & \text{on } \Gamma_M, \\ -k \partial_{\mathbf{n}} p = h_C p & \text{on } \Gamma_C. \end{cases} \quad (13)$$

The variational formulation of equation (13) reads as follows: find $p \in W(\Omega)$ such that

$$\int_{\Omega} k \nabla p \cdot \nabla \varphi dx + \int_{\Gamma_M} (h_M p + u - u_M) \varphi ds + \int_{\Gamma_C} h_C p \varphi ds = 0, \quad (14)$$

for all $\varphi \in W(\Omega)$. The existence of unique solution to system (14) can easily be verified through the application of Lax-Milgram lemma.

In summary, the following result is established.

Proposition 1 *The functional $\mathcal{J}(\Gamma_C)$ given by*

$$\mathcal{J}(\Gamma_C) = \min_{\varphi \in H^1(\Omega)} \sup_{\psi \in W(\Omega)} \mathcal{G}(\Omega, \varphi, \psi) \quad (15)$$

has the unique saddle point (u, p) which is completely characterized by systems (2) and (13).

The previous analysis also holds in the transformed domain Ω_t under the action of a velocity field \mathbf{V} for $t \geq 0$, i.e., we have

$$\mathcal{J}(\Gamma_{C_t}) = \min_{\varphi \in H^1(\Omega_t)} \sup_{\psi \in W(\Omega_t)} \mathcal{G}(\Omega_t, \varphi, \psi) \quad (16)$$

whose unique saddle point $(u_t, p_t) \in H^1(\Omega_t) \times W(\Omega_t)$ is characterized by

$$\mathcal{L}(\Omega_t, u_t, \varphi) = 0, \quad \forall \varphi \in W(\Omega_t), \quad (17)$$

$$d_\varphi \mathcal{F}(\Omega_t, u_t; \varphi) + d_\varphi \mathcal{L}(\Omega_t, u_t, p_t; \varphi) = 0, \quad \forall \varphi \in W(\Omega_t). \quad (18)$$

In the next section we discuss how the right side of equation (16) can be utilized to find the shape derivative of $\mathcal{J}(\Gamma_C)$.

3.2 Formal application of Correa-Seeger theorem.

The first-order shape derivative $d\mathcal{J}(\Gamma_C)[\mathbf{V}]$ of $\mathcal{J}(\Gamma_C)$, along the velocity field \mathbf{V} , can be obtain by evaluating the limit $dj(0) = \lim_{t \searrow 0} [j(t) - j(0)]/t$ where $j(t) := \mathcal{J}(\Gamma_{C_t})$. In view of (15) and (16), this can be accomplished by taking the derivative of the min-max functional $\mathcal{G}(\Omega_t, \varphi, \psi)$ with respect to the parameter $t \geq 0$. Such technique is, in particular, applicable to linear PDEs and convex cost functions (see, e.g., [46,47]). To accomplish the task, we need a theorem that would give the derivative of the minimax with respect to the parameter $t \geq 0$ at $t = 0$. Fortunately, a theorem due to Correa and Seeger [21] is already at our disposal, providing us a powerful tool to fulfil the task. However, the theorem cannot be directly applied to our case because of the ‘time’ dependence of the underlying function spaces appearing in the minimax formulation (16) (note that the Sobolev spaces $H^1(\Omega_t)$ and $W(\Omega_t)$ both depend on t). To address this issue and obtain an infimum with respect to a function space that is independent of t , we can use one of the two strategies offered in [22], namely: (i) function space parametrization technique and (ii) function space embedding technique.

For the computation of the shape gradient, we shall use the first mentioned technique. The technique consists of transporting the quantities defined in the variable domain Ω_t back onto the reference domain Ω . Once it is employed, the usual methods in differential calculus can now be applied since the functionals involved are now defined in a fixed domain Ω . The idea is to parametrize the functions in $H^1(\Omega_t)$ by elements of $H^1(\Omega)$ through the transformation $\varphi \mapsto \varphi \circ T_t^{-1} : H^1(\Omega) \rightarrow H^1(\Omega_t)$. Since T_t and T_t^{-1} are diffeomorphisms (cf. [9, Theorem 7]), it transforms the domain Ω onto Ω_t and changes the boundary Γ_{C_t} to Γ_C , noting Γ is fixed. In particular, since \mathbf{V} is a $C^{1,1}$ regular, we have $\varphi \circ T_t^{-1} \in H^1(\Omega_t)$ for all $\varphi \in H^1(\Omega)$, and conversely, $\psi \circ T_t \in H^1(\Omega)$ for all $\psi \in H^1(\Omega_t)$. Also, we introduce the parametrization

$H_{\Gamma_p,0}^1(\Omega_t) = \{\varphi \circ T_t^{-1} : \varphi \in W(\Omega)\}$. These parametrizations do not affect the value of the minimum of $\mathcal{J}(\Gamma_{C_t})$ but changes the Lagrangian functional \mathcal{G} :

$$\mathcal{J}(\Gamma_{C_t}) = \min_{\varphi \in H^1(\Omega)} \sup_{\psi \in W(\Omega)} \mathcal{G}(\Omega_t, \varphi \circ T_t^{-1}, \psi \circ T_t^{-1}).$$

Given the above functional, we define the new Lagrangian

$$\tilde{\mathcal{G}}(t, \varphi, \psi) := \mathcal{G}(\Omega_t, \varphi \circ T_t^{-1}, \psi \circ T_t^{-1}) = \mathcal{F}(\Omega_t, \varphi \circ T_t^{-1}) + \mathcal{L}(\Omega_t, \varphi \circ T_t^{-1}, \psi \circ T_t^{-1}), \quad (19)$$

for $\varphi \in H^1(\Omega)$ and $\psi \in W(\Omega)$. The unique saddle point $(u^t, p^t) \in H^1(\Omega) \times W(\Omega)$ of this new Lagrangian satisfies the equations

$$\mathcal{L}(\Omega_t, u^t \circ T_t^{-1}, \varphi \circ T_t^{-1}) = 0, \quad (20)$$

$$d_\varphi \mathcal{F}(\Omega_t, u^t \circ T_t^{-1}; \varphi \circ T_t^{-1}) + d_\varphi \mathcal{L}(\Omega_t, u^t \circ T_t^{-1}, p^t \circ T_t^{-1}; \varphi \circ T_t^{-1}) = 0, \quad (21)$$

for all $\varphi \in W(\Omega)$.

Remark 1 Comparing these expressions with the characterization of the minimizing element (u_t, p_t) of $\mathcal{G}(\Omega_t, \cdot, \cdot)$ on $H^1(\Omega_t) \times W(\Omega_t)$ which satisfies equations (17) and (18), we see that $u_t = u^t \circ T_t^{-1}$, $u^t = u_t \circ T_t$, $p_t = p^t \circ T_t^{-1}$ and $p^t = p_t \circ T_t$. So, (u^t, p^t) is actually the solution (u_t, p_t) of equations (17) and (18) in Ω_t transported back onto the fixed domain Ω by the change of variables induced by the transformation T_t . In particular, since $u_t \in W_{up}(\Omega_t)$, we see that u^t is in $W_{up}(\Omega)$.

Using domain and boundary transformations from Lemma 1, we can rewrite the Lagrangian $\tilde{\mathcal{G}}$ on Ω as

$$\tilde{\mathcal{G}}(t, \varphi, \psi) = \tilde{\mathcal{F}}(t, \varphi) + \tilde{\mathcal{L}}(t, \varphi, \psi), \quad (22)$$

where

$$\begin{aligned} \tilde{\mathcal{F}}(t, \varphi) &= \frac{1}{2} \int_{\Gamma_M} w_t (\varphi - u_M)^2 ds \\ \tilde{\mathcal{L}}(t, \varphi, \psi) &= \int_{\Omega} k A_t \nabla \varphi \cdot \nabla \psi dx + \int_{\Gamma_p} w_t (\varphi - u_p) \partial_n \psi ds + \int_{\Gamma_M} w_t [h_M (\varphi - u_\infty) - Q_M] \psi ds \\ &\quad + \int_{\Gamma_C} w_t [h_C (\varphi - u_C) - Q_C] \psi ds. \end{aligned}$$

The unique saddle point of this Lagrangian still satisfies equations (20) and (21) whose domain of integration can also be transported back to Ω using Lemma 1. More precisely, the unique saddle point $(u^t, p^t) \in H^1(\Omega) \times W(\Omega)$ of $\tilde{\mathcal{G}}$ satisfies

$$\tilde{\mathcal{L}}(t, u^t, \varphi) = 0, \quad \forall \varphi \in W(\Omega), \quad (23)$$

$$d_\varphi \tilde{\mathcal{F}}(t, u^t; \varphi) + d_\varphi \tilde{\mathcal{L}}(t, u^t, p^t; \varphi) = 0, \quad \forall \varphi \in W(\Omega). \quad (24)$$

Henceforth we will employ the theorem of Correa and Seeger [21] (see Theorem 1 in Appendix) to establish the shape derivative of $\mathcal{J}(\Gamma_C)$. The theorem actually provides conditions which allows to conclude the equality $d\mathcal{J}(\Gamma_C)[\mathbf{V}] = \partial_t \tilde{\mathcal{G}}(t, u, p)|_{t=0}$ without employing the *material derivative* of the state variable (see, e.g., [9, Definition 12]). The application of the theorem particularly demands the verifications of four conditions (H1)–(H4) in Theorem 1. Following the ideas issued in [22, Section 5.5], these conditions of the theorem are easily

satisfied as attested in the Appendix. Hence, we can conclude from Theorem 1 that the shape derivative of $\mathcal{J}(\Gamma_C)$, along a deformation field $\mathbf{V} \in \Theta_1$, is given by

$$d\mathcal{J}(\Gamma_C)[\mathbf{V}] = \partial_t \tilde{\mathcal{G}}(t, u, p)|_{t=0} = \int_{\Omega} k A'_0 \nabla u \cdot \nabla p \, dx + \int_{\Gamma_C} w'_0 \{h_C(u - u_C) - Q_C\} p \, ds, \quad (25)$$

where $A'_0 = \operatorname{div} \mathbf{V} \mathbf{I}_2 - D\mathbf{V} - (D\mathbf{V})^T$ and $w'_0 = \operatorname{div}_{\Gamma} \mathbf{V}$. Notice that the above expression for the shape gradient of $\mathcal{J}(\Gamma_C)$ is composed of a volume and a boundary integral. This expression, however, can be further simplified and expressed in terms of just a boundary integral, but this additional property requires higher regularity of the state and adjoint state variables u and p . We emphasize that the derivative $d\mathcal{J}(\Gamma_C)[\mathbf{V}]$ does exist for all $\mathbf{V} \in \Theta_1$ and the mapping $\mathbf{V} \rightarrow d\mathcal{J}(\Gamma_C)[\mathbf{V}] : \Theta_1 \rightarrow \mathbb{R}$ is linear and continuous (cf. [10]). Hence, according to Zolésio-Hadamard structure theorem [22, Theorem 3.6, Section 3.4], there is a function \mathbb{G}_{Ω} defined on the boundary Γ_C (i.e., a scalar distribution g in $\mathcal{D}'(\Gamma_C)$) such that $d\mathcal{J}(\Gamma_C)[\mathbf{V}] = \int_{\Gamma_C} \mathbb{G}_{\Omega} \mathbf{V} \cdot \mathbf{n} \, ds$. The boundary expression for the shape gradient can be obtained by applying the identities in Lemma 2 and Lemma 3. The application of Lemma 2, however, is not straightforward because of the singularity appearing at the transition points between Γ_P and Γ_M . To handle such issue, we can combine the ideas developed in [12, 42, 51] to control the singularities appearing on the fixed boundary Γ and arrive at a related problem corresponding to (2) and (13) with the same boundary condition on Γ_C . As a result, the weak formulation corresponding to these new PDE systems respectively admits a unique solution possessing the higher regularity H^2 . Since the perturbation field \mathbf{V} vanishes on Γ , then, even if we subtract off the singularities on the boundary condition specified on the known boundary Γ , the resulting expression for the shape gradient will still consists of only the integrals defined over the free boundary Γ_C . Denoting the H^2 regular solutions of the controlled PDE systems corresponding to (2) and (13) by \tilde{u} and \tilde{p} , respectively, we can show that, on the free boundary Γ_C , we have $\tilde{u} = u$ and $\tilde{p} = p$. By these arguments, we can now apply Lemma 2 and Lemma 3 to (25), and finally write $d\mathcal{J}(\Gamma_C)[\mathbf{V}]$ as the boundary integral

$$\begin{aligned} d\mathcal{J}(\Gamma_C)[\mathbf{V}] &= \int_{\Gamma_C} k(\nabla u \cdot \nabla p) \mathbf{V} \cdot \mathbf{n} \, ds + \int_{\Gamma_C} (h_C(u - u_C) - Q_C) (\mathbf{V} \cdot \nabla p) \, ds \\ &\quad + \int_{\Gamma_C} h_C p (\mathbf{V} \cdot \nabla u) \, ds + \int_{\Gamma_C} \partial_{\mathbf{n}} [(h_C(u - u_C) - Q_C) p] \mathbf{V} \cdot \mathbf{n} \, ds \\ &\quad + \int_{\Gamma_C} \kappa (h_C(u - u_C) - Q_C) p \mathbf{V} \cdot \mathbf{n} \, ds - \int_{\Gamma_C} \mathbf{V} \cdot \nabla [(h_C(u - u_C) - Q_C) p] \, ds \\ &= \int_{\Gamma_C} k(\nabla u \cdot \nabla p) \mathbf{V} \cdot \mathbf{n} \, ds + \int_{\Gamma_C} \partial_{\mathbf{n}} p (h_C(u - u_C) - Q_C) \mathbf{V} \cdot \mathbf{n} \, ds \\ &\quad + \int_{\Gamma_C} [h_C p \partial_{\mathbf{n}} u + \kappa (h_C(u - u_C) - Q_C) p] \mathbf{V} \cdot \mathbf{n} \, ds. \end{aligned}$$

By writing $\mathbb{G} := \mathbb{G}_{\Omega}$ as

$$\mathbb{G} = k \nabla u \cdot \nabla p + k \partial_{\mathbf{n}} p (h_C(u - u_C) - Q_C) + h_C p \partial_{\mathbf{n}} u + \kappa (h_C(u - u_C) - Q_C) p, \quad (26)$$

we see that, indeed, the shape derivative of the cost function $\mathcal{J}(\Gamma_C)$ along a deformation field \mathbf{V} over Ω can be expressed as $d\mathcal{J}(\Gamma_C)[\mathbf{V}] = \int_{\Gamma_C} \mathbb{G} \mathbf{V} \cdot \mathbf{n} \, ds$.

We formalize our result in the following proposition.

Proposition 2 Let $\Omega \subset \mathbb{R}^2$ be a doubly connected, bounded $C^{1,1}$ domain with boundary $\partial\Omega = \bar{\Gamma}_P \cup \bar{\Gamma}_M \cup \Gamma_C$ and $\mathbf{V} \in \Theta_1$. Then, the cost functional

$$\mathcal{J}(\Gamma_C) = \frac{1}{2} \int_{\Gamma_M} (u - u_M)^2 ds,$$

where u satisfies the state problem (2), is shape differentiable. Moreover, for a given velocity field $\mathbf{V} \in \Theta_1$, its derivative $d\mathcal{J}(\Gamma_C)[\mathbf{V}]$ in boundary integral form is given by

$$\begin{aligned} d\mathcal{J}(\Gamma_C)[\mathbf{V}] &= \int_{\Gamma_C} k(\nabla u \cdot \nabla p) \mathbf{V} \cdot \mathbf{n} ds + \int_{\Gamma_C} \partial_{\mathbf{n}} p (h_C(u - u_C) - Q_C) \mathbf{V} \cdot \mathbf{n} ds \\ &\quad + \int_{\Gamma_C} [h_C p \partial_{\mathbf{n}} u + \kappa (h_C(u - u_C) - Q_C) p] \mathbf{V} \cdot \mathbf{n} ds, \end{aligned} \quad (27)$$

where the adjoint state p satisfies the adjoint state problem (13), and κ represents the mean curvature of Γ_C .

The computational strategy issued above can easily be adapted to establish the shape gradient of the Neumann-data-tracking cost functional $\mathcal{J}_N(\Gamma_C)$ for the corrosion detection problem. Indeed, considering that the solution u_D of the state problem (3) has an H^3 regularity, then one establishes the following result.

Proposition 3 Let $\Omega \subset U \subset \mathbb{R}^2$ be a connected, bounded $C^{2,1}$ domain with boundary $\partial\Omega = \Gamma \cup \Gamma_C$. For a given velocity field $\mathbf{V} \in \Upsilon_N$, where

$$\Upsilon_N := \{\mathbf{V}(t, x) \in C^{2,1}([0, \varepsilon_N] \times \bar{\Omega}, \mathbb{R}^2) : \mathbf{V}|_{\Gamma \cup \partial U} = 0\},$$

the shape functional $\mathcal{J}_N(\Gamma_C) = \frac{1}{2} \int_{\Gamma} (\partial_{\mathbf{n}} u_D - g)^2 ds$ is shape differentiable with

$$d\mathcal{J}_N(\Gamma_C)[\mathbf{V}] = \int_{\Gamma_C} [\nabla u_D \cdot \nabla p_D + (\kappa \lambda - 2\lambda^2) u_D p_D] \mathbf{V} \cdot \mathbf{n} ds. \quad (28)$$

Here, the state variable u_D is the unique solution of (3) with $f \in H^{\frac{1}{2}}(\Gamma)$, and p_D represents the adjoint state variable which is the only solution to the BVP

$$-\Delta p_D = 0 \text{ in } \Omega, \quad p_D = -(\partial_{\mathbf{n}} u_D - g) \text{ on } \Gamma, \quad \partial_{\mathbf{n}} p_D + \lambda p_D = 0 \text{ on } \Gamma_C. \quad (29)$$

In above result, the set U is a connected bounded domain in \mathbb{R}^2 containing all deformations of Ω under the transformation T_t and hence, is called as the *hold-all* or *universal domain*. We point out that the H^3 regularity of the state solution u_D and the adjoint state solution p_D can only be guaranteed when Ω is $C^{2,1}$ regular and, in addition, the observable boundary is disjoint with the unknown boundary Γ_C , i.e., $\text{dist}(\Gamma, \Gamma_C) > 0$. If, however, $\Gamma_C = \partial\Omega \setminus \bar{\Gamma}$, then u_D and p_D do not have higher regularity and are only elements of $H^1(\Omega)$. Nevertheless, a similar treatment (removing the singularities appearing on Γ) in the case of cavity detection problem can be applied to get higher regularity for u_D and p_D .

Meanwhile, when the Neumann problem

$$-\Delta u_N = 0 \text{ in } \Omega, \quad \partial_{\mathbf{n}} u_N = g \text{ on } \Gamma, \quad \partial_{\mathbf{n}} u_N + \lambda u_N = 0 \text{ on } \Gamma_C, \quad (30)$$

is given, the Dirichlet data can be tracked in a least-squares sense relative to $L^2(\Gamma)$ and we may consider the minimization problem

$$\min_{\Gamma_C \in \bar{\partial}_{\text{ad}}} \left\{ \mathcal{J}_D(\Gamma_C) := \frac{1}{2} \int_{\Gamma} (u_N - f)^2 ds \right\}, \quad (31)$$

where $\tilde{\mathcal{O}}_{\text{ad}}$ is some admissible set of geometries. In this case, the assumption that Ω is of class $C^{1,1}$, with boundary $\partial\Omega = \Gamma \cup \Gamma_C$ where $\Gamma \cap \Gamma_C = \emptyset$, and $g \in H^{3/2}(\Gamma)$, is sufficient to establish the boundary expression for the shape gradient of $\mathcal{J}_D(\Gamma_C)$; that is, we have the following proposition.

Proposition 4 *Let $\Omega \subset U \subset \mathbb{R}^2$ be a connected, bounded $C^{1,1}$ domain with boundary $\partial\Omega = \Gamma \cup \Gamma_C$. For a given velocity field $\mathbf{V} \in \Upsilon_D$, where*

$$\Upsilon_D := \{\mathbf{V}(t, x) \in C^{1,1}([0, \varepsilon_D] \times \overline{\Omega}, \mathbb{R}^2) : \mathbf{V}|_{\Gamma \cup \partial U} = 0\},$$

the shape functional $\mathcal{J}_D(\Gamma_C) = \frac{1}{2} \int_{\Gamma} (u_N - f)^2 ds$ is shape differentiable with

$$d \mathcal{J}_D(\Gamma_C)[\mathbf{V}] = \int_{\Gamma_C} [\nabla u_N \cdot \nabla p_N + (\kappa\lambda - 2\lambda^2)u_N p_N] \mathbf{V} \cdot \mathbf{n} ds. \quad (32)$$

Here the state variable u_N is the unique solution of (30) with $g \in H^{3/2}(\Gamma)$, and p_N denotes the adjoint state variable which is the only solution to the BVP

$$-\Delta p_N = 0 \text{ in } \Omega, \quad p_N = -(u_N - f) \text{ on } \Gamma, \quad \partial_{\mathbf{n}} p_N + \lambda p_N = 0 \text{ on } \Gamma_C. \quad (33)$$

Again, we point out that the assumption that Γ_C and Γ are disjoint is vital in securing higher regularity for the solutions of the variational formulations corresponding to the PDE systems (30) and (33). In the case when $\Gamma_C = \partial\Omega \setminus \bar{\Gamma}$, the lack of higher regularity of u_N and p_N again arise. Nevertheless, and as we mentioned before, such issue can be treated with the aid of the results exhibited in [12, 42, 51]. Further investigation regarding this problem will be the subject of our future work.

Now, the computed boundary expression for the shape gradient of the cost function $\mathcal{J}(\Gamma_C)$ (resp. $\mathcal{J}_N(\Gamma_C)$ and $\mathcal{J}_D(\Gamma_C)$) allows us to numerically solve the minimization problem (4) (resp. (5) and (31)) by means of a gradient-based scheme. In the next section, we will describe an iterative process, employing a boundary variation algorithm based on the H^1 gradient method, to solve the minimization problem (4). Then, we will illustrate its feasibility by solving various numerical examples.

4 Numerical Approximation

It is well-known that geometric inverse problems, such as the identification of defects, are ill-posed. In most cases, especially when detection is carried out only through boundary measurements, one can expect a severely ill-posed problem without too accurate reconstructions of the exact solution [15].

Here we shall not tackle the issue of identifiability, rather we shall proceed directly on the numerical approximation procedure of the optimization problem. Nonetheless, we shall see in our numerical results that a single measurement provides good enough identifications of the cavities. As alluded in Introduction, an identifiability result concerning a related problem was recently proved by Bacchelli in [11] for Robin boundary conditions, and in the case of generalized impedance boundary condition, the problem was addressed by Cakoni et al. in [17]. Meanwhile, the question of existence of optimal solution for the shape optimization problem (4) subject to (2) can be treated in a similar fashion as in [49], exploiting the ideas furnished in [25] (but whose details will not be further issued here).

In the next section we discuss the method we use for the numerical realization of the optimization problem.

4.1 The H^1 Gradient Method

The iterative algorithm we use in our numerical experiment is based on the H^1 gradient method [3] (see also [4, 5, 7, 8]) which was motivated by the traction method introduced in [2]. For more details of this method (such as its application to optimal shape design problems), we refer the readers to the aforementioned papers.

As in most situations, the numerical solution of the minimization (4) comprises in adopting an iterative process that decreases the cost value $\mathcal{J}(\Gamma_C)$ at each iteration. Let us denote by Γ_C^k the boundary of the cavity at the k -th iteration. Then, at the $(k+1)$ -th iterative step, the boundary Γ_C^{k+1} becomes $\Gamma_C^{k+1} = \{x + t\mathbf{V}_k(x) : x \in \Gamma_C^k\}$, where $t \geq 0$ is a sufficiently small step size parameter. The deformation field \mathbf{V} is chosen such that it provides a decent direction for the cost functional $\mathcal{J}(\Gamma_C)$. Referring to [5], if such a \mathbf{V} exists, then it should satisfy

$$\langle \mathbf{V}, \varphi \rangle_{\mathcal{X}} = -\langle \mathbb{G}\mathbf{n}, \varphi \rangle_{L^2(\Gamma_C)}, \quad (34)$$

where \mathbb{G} denotes the kernel of the shape gradient given by (26), for all φ taken from some appropriately chosen functional space \mathcal{X} . The choice of the scalar product in (34) is crucial for the development of an efficient numerical scheme for shape optimization problems. In [4], the authors proposed the traction method [2] to address some irregularity issues in shape optimization problems. This approach is based from the regularization of the descent direction by means of a scalar product inspired by the linear elasticity equation. Quite recently, a comparison of the L^2 , H^1 and H^{-1} scalar products defined on a surface was presented in [23]. The authors, however, commented that the best choice is strongly dependent on the application of interest. In [35], for instance, the author chose $\mathcal{X} := H^1(\Omega)$ to numerically solve a shape optimization problem derived from a free-surface problem.

If one chooses, for instance, $\mathcal{X} := L^2(\Gamma_C)$, then $\mathbf{V}|_{\Gamma_C} = -\mathbb{G}\mathbf{n}$, and for this choice of the function space, the shape gradient (27) is strictly negative. However, choosing \mathbf{V} in this way may result in subsequent loss of regularity of Γ_C , hence creating oscillations of Γ_C (cf. [45]). In fact, it is generally known that direct application of gradient method often leads to oscillating shapes [27] and these oscillations are actually caused by a lack of smoothness of the shape gradient [4, 45]. To address such issue in our numerical treatment, we need to apply regularization methods. This is usually achieved by adding additional stabilizing terms to the objective function, such as perimeter. Hence, taking into account these issuing facts, we compute \mathbf{V} through the H^1 gradient method introduced in [5], given as

$$\langle \mathbf{V}, \varphi \rangle_{H^1(\Omega)} = -\langle \mathbb{G}\mathbf{n}, \varphi \rangle_{L^2(\Gamma_C)}, \quad \forall \varphi \in \mathbf{H}^1(\Omega), \quad (35)$$

where $\mathbf{H}^1(\Omega) := \{\varphi = (\varphi_1, \varphi_2) : \varphi_1, \varphi_2 \in H^1(\Omega)\}$, coupled with perimeter penalization, to get rid of the irregularity issues arising in the shape optimization problem. With perimeter penalization, the cost function becomes $\mathcal{J}(\Gamma_C) + \beta \mathcal{P}(\Omega)$, where $\mathcal{P}(\Omega) := \int_{\partial\Omega} 1 \, ds$, whose corresponding first-order shape derivative, along some deformation field $\mathbf{V} \in \Theta_1$, is easily computed as $d\mathcal{P}(\Omega)[\mathbf{V}] = \int_{\Gamma_C} \kappa \mathbf{V} \cdot \mathbf{n} \, ds$. Here, $\beta \geq 0$ is some small fixed parameter. Given this new cost function, we define the kernel $\tilde{\mathbb{G}}$ as

$$\tilde{\mathbb{G}} := \mathbb{G} + \beta\kappa. \quad (36)$$

Here, we remark that the resulting deformation field \mathbf{V} (also referred to in some literature as the Sobolev gradient [43]) calculated using (34) with $\mathcal{X} := H^1(\Omega)$ actually produces an extension of $\mathbb{G}\mathbf{n}$ over the entire domain, which may be shown to have not only a regularizing effect on the boundary (cf. [45]) but also preconditions the descent direction [35].

4.2 The Boundary Variation Algorithm

Before giving the optimization algorithm, we remark that in view of the previous discussions, the exact minimization problem now reads as

$$\min_{\Omega \in \mathcal{O}_{\text{ad}}} \left\{ \frac{1}{2} \int_{\Gamma_M} (u_\Omega - u_M)^2 ds + \beta \int_{\partial\Omega} 1 ds \right\}, \quad (37)$$

where the state variable u_Ω satisfies the mixed BVP (2), and \mathcal{O}_{ad} denotes admissible set of geometries defined as

$$\mathcal{O}_{\text{ad}} = \left\{ \Omega \subset \mathbb{R}^2 : \Omega \text{ is a connected bounded } C^{1,1} \text{ domain, with boundary } \partial\Omega = \Gamma \cup \Gamma_C \text{ such that } \text{dist}(\Gamma, \Gamma_C) > d_0, \text{ for some small number } d_0 > 0 \right\}.$$

Now we give the optimization algorithm which is structured as follows:

Algorithm The boundary variation algorithm

- 1: Choose an initial shape Ω_0 ;
- 2: Solve the state equation (2) and adjoint state equation (13) on the current domain Ω_k using finite element;
- 3: Compute the descent direction \mathbf{V}_k by using (35), which amounts to solving the following system

$$-\Delta \mathbf{V} + \mathbf{V} = 0 \text{ in } \Omega, \quad \mathbf{V} = 0 \text{ on } \Gamma, \quad \partial_{\mathbf{n}} \mathbf{V} = -\tilde{\mathbf{G}} \mathbf{n} \text{ on } \Gamma_C,$$

with $\Omega = \Omega_k$;

- 4: Modify the current domain by \mathbf{V}_k to obtain a new domain Ω_{k+1} , i.e., set $\Omega_{k+1} := \{x + t_k \mathbf{V}_k(x) : x \in \Omega_k\}$, for some sufficiently small scalar $t_k > 0$.
-

We implement the above algorithm in FREEFEM++ [26] with the following general setup. In Step 2, we use a P2 finite elements discretization to solve the state equation (2) and adjoint state equation (13). In Step 3, we choose the penalization parameter $\beta \geq 0$ by trial and error, and we set its value as small as possible. Meanwhile, the choice of the descent step size t_k is not an easy task. If t_k is too big, the algorithm is unstable and causes the solver to crash; if it is too small, the rate of convergence is insignificant. To overcome this difficulty, we will choose the step size t_k in Step 4 on the basis of the scalar product $\langle \mathbf{V}_k, \mathbf{V}_{k-1} \rangle_{H^1(\Omega)} =: \eta$. We explained this as follows. We suspect that when η takes a negative value, the algorithm is becoming unstable. In this case, we reduce t_k (exactly by half) and initialize the next iteration with the previous shape $\Omega^{(k-1)}$. Contrary-wise, if η is positive, we increase the step size parameter t_k (i.e., we set $t_{k+1} = (1 + \rho)t_k, t_0 = \rho/10, \rho \in \{0.1, 0.01\}$). Moreover, the step t_k is also decreased whenever there are reversed triangles within the mesh after the update (this is done through the built-in function *adaptmesh* which is use to refine and avoid degeneracy of the triangles in the meshes). Lastly, we vary the shape of Ω using *movemesh* (which is also a function in FREEFEM++ that applies a global diffeomorphism to the mesh).

Regarding the computation of the deformation field \mathbf{V} in Step 3, notice that the kernel $\tilde{\mathbf{G}}$ given in (36) involves the expression for the mean curvature κ of the boundary of the cavity Γ_C . In this work, we propose to apply the idea of the H^1 gradient method with Robin condition [5] in order to obtain a smooth extension of the normal vector field \mathbf{n} for the computation of the mean curvature κ . The working equation is similar to the one used in [35] in computing the mean curvature in the context of free surface problems, but differs,

however, in the domain of integration for the bilinear form of the first derivative. To state more precisely, we evaluate the mean curvature as

$$\kappa := \operatorname{div}_{\Gamma_C}(\mathbf{n}_\varepsilon),$$

where $\mathbf{n}_\varepsilon \in \mathbf{H}^1(\Omega)$ is the smoothed (harmonic) extension of the normal vector field satisfying

$$\int_{\Omega} \varepsilon \nabla \mathbf{n}_\varepsilon : \nabla \boldsymbol{\varphi} \, dx + \int_{\Gamma_C} \mathbf{n}_\varepsilon \cdot \boldsymbol{\varphi} \, ds = \int_{\Gamma_C} \mathbf{n} \cdot \boldsymbol{\varphi} \, ds, \quad \forall \boldsymbol{\varphi} \in \mathbf{H}^1(\Omega), \quad (38)$$

and $\varepsilon > 0$ is some fixed small parameter, and the tensor scalar product $\nabla \mathbf{n}_\varepsilon : \nabla \boldsymbol{\varphi}$ is given by $\nabla \mathbf{n}_\varepsilon : \nabla \boldsymbol{\varphi} = \sum_{i,j=1}^2 \frac{\partial n_{\varepsilon j}}{\partial x_i} \frac{\partial \varphi_j}{\partial x_i} \in \mathbb{R}$. In all test cases we present here, we set $\varepsilon = 0.0001$ in (38) for the computation of the mean curvature κ .

4.3 Stopping Criterion

Finally, to complete the algorithm, we need to specify how the iteration process shall be terminated. Typically, an optimization loop for shape optimization problems is stopped when the cost function reaches a certain small value or whether the shape gradients in some suitable norm are small enough. However, in the case of geometric inverse problems, it would be better to rely on the notion of distances between sets. The most common choice would be the concept of Hausdorff distance. It is defined for two sets $\Omega_1, \Omega_2 \subset \mathbb{R}^2$ by

$$\operatorname{dist}_H(\Omega_1, \Omega_2) = \sup \left\{ \sup_{x \in \Omega_1} \operatorname{dist}(x, \Omega_2), \sup_{y \in \Omega_2} \operatorname{dist}(\Omega_1, y) \right\}$$

where $\operatorname{dist}(x, \Omega_2) = \min_{y \in \Omega_2} |x - y|$. Hence, a good candidate for the stopping criterion of the algorithm would be the inequality condition $\operatorname{dist}_H(\Gamma_C^k, \Gamma_C^{k-1}) < C(\delta x)^2$, where C is a constant independent of the grid parameter δx . Here, noting that $\Gamma_C^k = \{x + t_{k-1} \mathbf{V}_{k-1}(x) : x \in \Gamma_C^{k-1}\}$, we use the H^1 norm of \mathbf{V} and the step size parameter t as a stopping criterion for the algorithm; that is, we terminate the algorithm as soon as the inequality condition

$$t_k \|\mathbf{V}_k\|_{H^1(\Omega)} < \theta, \quad (39)$$

is satisfied for some small value $\theta > 0$.

5 Numerical Results

For the numerical experiments, we consider the shape optimization problem (1) subject to (2) with the following broad assumptions. The object being examined has a circular shape having a unit radius (centered at the origin). We assume that the two dimensional object has thermal conductivity k of 1.0 W/mK, and its outer boundary Γ_M has a convective heat transfer with $h_M = 1.1$ W/mK and surrounding temperature of $u_\infty = 27$ °C. Meanwhile, the remaining outer part Γ_P is heated with prescribed temperature $u_P = 40$ °C. Moreover, in the interior part of the cavity, the convective heat transfer measures $h_C = 0.7$ W/mK, and $u_C = 22$ °C. Lastly, zero heat fluxes Q_M and Q_C are assumed in all of the following examples.

For the extra temperature measurements on the outer part Γ_M of the boundary, we use synthetic data; that is, the temperature distribution u_M measured on the accessible boundary Γ_M is generated by numerically solving the forward problem (1) using finite element method.

To avoid ‘inverse crimes’ (see comments by Colton and Kress [20, p. 133]) in producing the measurements, we generate the synthetic data with a different numerical scheme (i.e., using a different number of discretization points and applying P3 finite element basis functions in the FREEFEM++ code) than in the inversion process. Then, we extract the measurement u_M by computing u on Γ_M . For the tests with noise, we perturbed the data by Gaussian noise. Moreover, for simplicity, we assume that the unknown cavity Γ_C can be represented in polar coordinates.

Finally, to illustrate the feasibility of the proposed method as described in previous sections, the identification procedure is tested by several cavity detection problems which we detail in the following test cases.

5.1 First case: influence of the initial guess

First we examine the effect of the initial shape on the identified cavity. We let the boundary of the exact cavity $\Gamma_C := \Gamma_C^{\text{exact}}$ be parametrically given as

$$\Gamma_C = \left\{ \begin{pmatrix} 0.3 + 0.3 \cos t \\ 0.3 \sin t \end{pmatrix}, \forall t \in [0, 2\pi) \right\}.$$

The numerical results, with different initial guesses, are shown in Figure 1. Here, we ignore, for the meantime, the stopping criterion (39) and fix the number of iterations. This simple condition, however, permits us to obtain effective results for the present objective. In these test cases, we observed that the different choices of the initial guess will affect the required number of iterations. In these situations, however, the solutions finally converge to the exact location of the cavity within a finite number of iterations. Figure 1a shows the history of (selected) approximated shapes until 300 iterations wherein the initial guess is given by

$$\Gamma_C^0 = \left\{ 0.9 \begin{pmatrix} \cos t \\ \sin t \end{pmatrix}, t \in [0, 2\pi) \right\}.$$

With this initial guess, we are able to obtain a reasonable identification of the cavity. Meanwhile, referring to Figure 1b, setting the initial shape to

$$\Gamma_C^0 = \left\{ 0.5 \begin{pmatrix} \cos t \\ \sin t \end{pmatrix}, t \in [0, 2\pi) \right\},$$

only provides a good location of the identified cavity. After 100 iterations we obtained a cavity shape (almost) indistinguishable from the one depicted in Figure 1b where it shows the reconstructed cavity after 300 iterations. Based on the history of values for the relative residuum $\|u - u_M\|_{L^2(\Gamma_M)} / \|u_M\|_{L^2(\Gamma_M)}$ (computed during each iterative step, including the reinitialization of $\Omega^{(k)}$) shown in Figure 1c, further iterations of our numerical scheme beyond 100 iterative steps will no longer provide better reconstruction of the cavity since the value of the residuum only oscillates at some fixed number at larger iterations. This observation is further confirmed by the history of values for the Hausdorff distance of the approximate shapes against the exact shape of the cavity represented by Γ_C^{exact} at each iteration (refer to Figure 1c). We believe that this difficulty is due to how the synthetic data was generated in the numerical computations and the severity of the ill-posedness of the problem. Building on this illustrated example, we hypothesize that it is difficult to guarantee that in all cases the final shape will be independent of the initial guess. Nevertheless, we can at

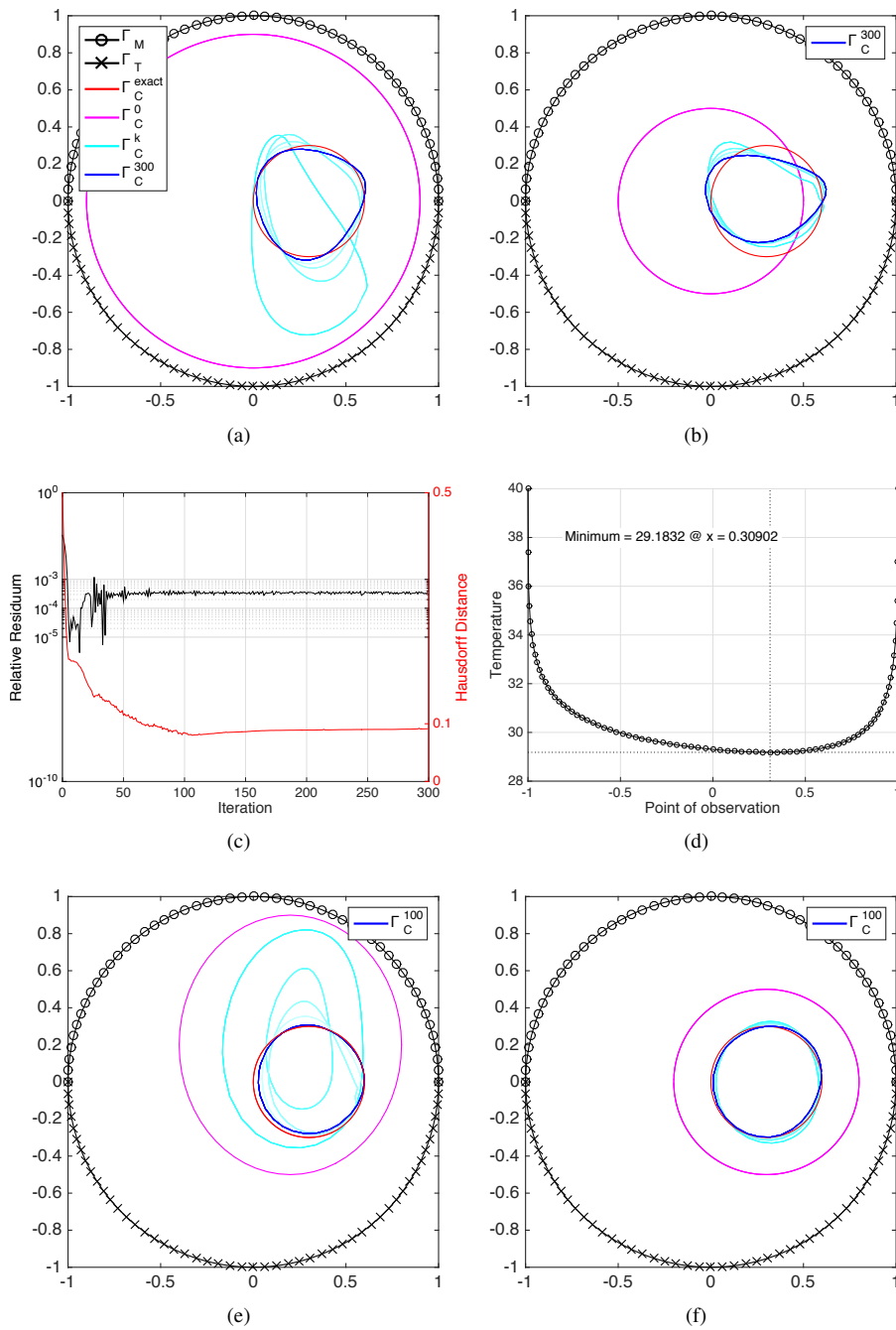


Fig. 1: (a)-(b), (e)-(f): Detection of a circular cavity with different initial guesses; (c) history of relative residuum $\|u - u_M\|_{L^2(\Gamma_M)} / \|u_M\|_{L^2(\Gamma_M)}$ and Hausdorff distance $\text{dist}_H(\Gamma_C^k, \Gamma_C^{\text{exact}})$ for the test result depicted in (b); (d) temperature pattern on the observable boundary Γ_M .

least reduce the number of iterations and possibly obtain better approximations by setting a good location for the initial guess. This can be done by exploiting the temperature pattern on the observable boundary Γ_M where measurement is performed. Using this thermal pattern, we can guess which section of the specimen the cavity might be located, however, we cannot exactly estimate how deep the cavity is.

In the present test case, the temperature distribution on the boundary Γ_M is shown in Figure 1d. At approximately $x = 0.31$, we see a minimum value of 29.18 °C for the temperature. This indicates (at least in the case of noised-free synthetic data) that a cavity is present along this axis. Hence, it would be ideal to set an initial guess along this section of the object. Two additional identification processes with initial guesses given by

$$\Gamma_C^0 = \left\{ \begin{pmatrix} 0.2 + 0.6 \cos t \\ 0.2 + 0.7 \sin t \end{pmatrix}, t \in [0, 2\pi) \right\}, \quad \Gamma_C^0 = \left\{ \begin{pmatrix} 0.3 + 0.3 \cos t \\ 0.3 \sin t \end{pmatrix}, t \in [0, 2\pi) \right\}$$

are respectively shown in Figure 1e and Figure 1f. These choices of the initial shape for the identification process improved the computed shape of the cavity as evident in the latter two figures.

A priori information about the size and depth of the cavity. In practice, the size and depth of the defect makes the imaging process more difficult (see [38]) especially when only a part of the specimen is subject for testing and evaluation. In the first test case above, we have already used the thermal distribution on Γ_M to guess which section of the specimen the cavity might be located. This information can be further exploited, at least to some extent, to obtain some knowledge about the size and depth of the cavity. To do so, we first examine some few test cases and see the effect of the size and location of the cavity on the observed thermal pattern on Γ_M . For this purpose, we consider, for $k \in \{0, 1, 2, 3, 4\}$ and $l \in \{0, 1, 2\}$, the following parametrization of the exact cavities:

$$\begin{aligned} \Gamma_{C,k}^{SV} &= \left\{ \begin{pmatrix} 0.15 \cos t \\ -0.8 + 0.4k + 0.15 \sin t \end{pmatrix}, t \in [0, 2\pi) \right\}, \\ \Gamma_{C,k}^{SH} &= \left\{ \begin{pmatrix} (-0.8 + 0.4k) + 0.15 \cos t \\ 0.15 \sin t \end{pmatrix}, t \in [0, 2\pi) \right\}, \\ \Gamma_{C,l}^{LV} &= \left\{ \begin{pmatrix} 0.45 \cos t \\ 0.5(l-1) + 0.45 \sin t \end{pmatrix}, t \in [0, 2\pi) \right\}, \\ \Gamma_{C,l}^{LH} &= \left\{ \begin{pmatrix} 0.5(l-1) + 0.45 \cos t \\ 0.45 \sin t \end{pmatrix}, t \in [0, 2\pi) \right\}. \end{aligned}$$

The exact geometries of the above shapes for all values of k and l are shown in Figure 2a and Figure 3a, for small and large cavities, respectively. The temperature patterns for the cavities $\Gamma_{C,k}^{SV}$ and $\Gamma_{C,k}^{SH}$ (running the values of k) are shown in Figure 2b and Figure 2c, respectively. On the other hand, the respective temperature patterns for the cavity $\Gamma_{C,l}^{LV}$ and $\Gamma_{C,l}^{LH}$ are depicted in Figure 3b and Figure 3c. The computed least temperature values on the boundary Γ_M for each of these test cases is depicted in Figure 2d for the first two test cases and Figure 3d for the last two scenarios. From these results, we have drawn the following observations (at least in the case of trivial shapes). Looking at Figure 2b and Figure 3b, we notice that as the cavity becomes closer to the region of measurement, the ‘flatness’ of the parabolic thermal plot at its vertex decreases, while its ‘curvature’ increases (i.e., becomes more pointed). In other words, the measured least temperature value on the section where the cavity might be situated is much lower compared to the measurements in its neighboring points of observation. Moreover, comparing the results shown in Figure

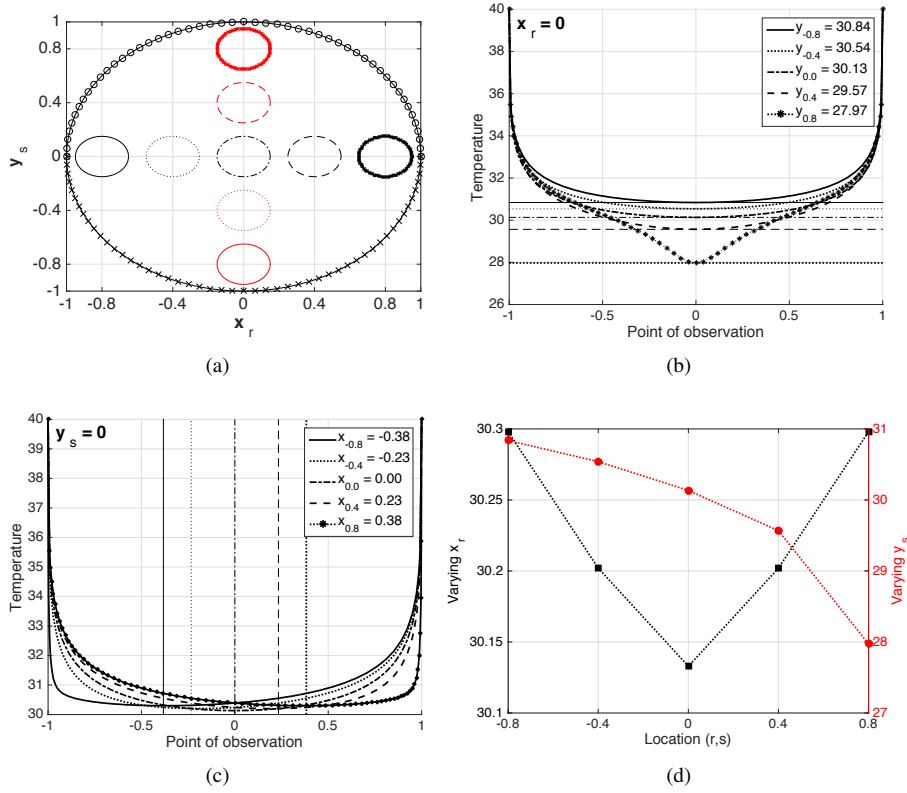


Fig. 2: (a): Exact geometries of the cavities $\Gamma_{C,k}^{SV}$ and $\Gamma_{C,k}^{SH}$, for all the given values of k ; (b): temperature pattern on Γ_M when the cavity is given by $\Gamma_{C,k}^{SV}$, for all the given values of k ; (c): temperature pattern on Γ_M when the cavity is given by $\Gamma_{C,k}^{SH}$, for all the given values of k ; (d): computed least value for each of the measured temperatures shown in (b) and (c).

2b and Figure 3b, we observe that a smaller size cavity produces a sharper temperature pattern compared to cavities with larger size. However, it seems that the size of cavity is more difficult to guess when the cavity is far from the region of measurement. Meanwhile, referring to Figure 2c and Figure 3c, we see that the temperature pattern clearly indicates which section of the specimen the cavity might be located. We shall use these informations in the numerical approximations of the succeeding test cases, particularly in specifying the stopping condition of the iterative process.

5.2 Second case: influence of the location and size of the cavity

For the second test case, we want to know the accuracy of the identification process with respect to the location and size of the cavity. We consider four different scenarios, the first two of which contains a large cavity with different locations, and the last two having a smaller cavity, again, with different locations. In particular, we consider the following descriptions

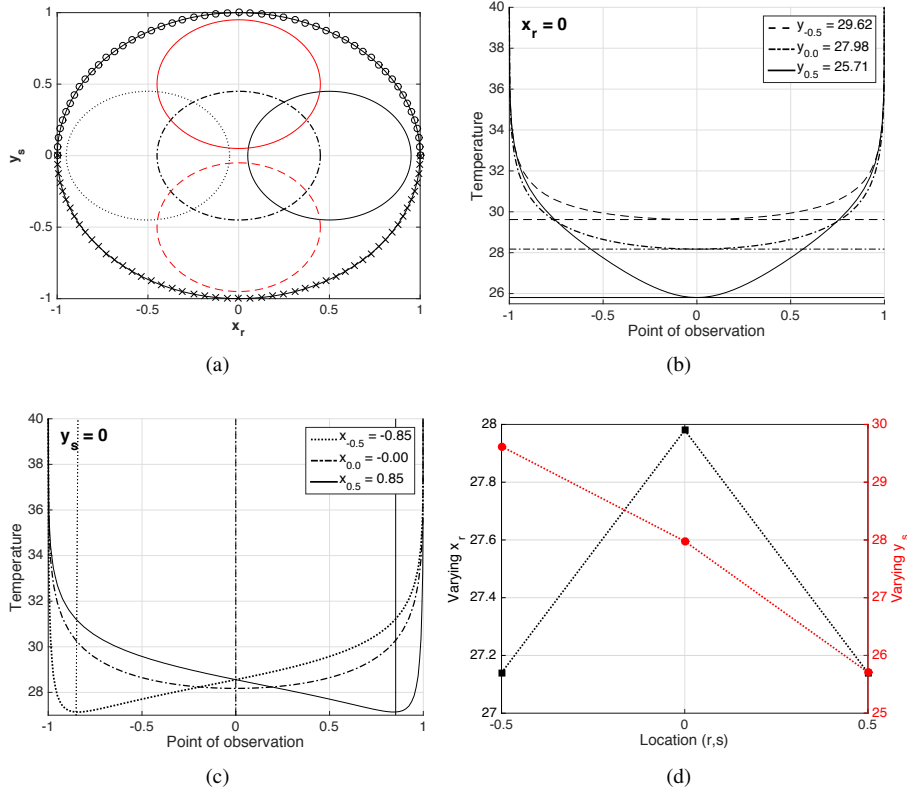


Fig. 3: (a): Exact geometries of the cavities $\Gamma_{C,l}^{LV}$ and $\Gamma_{C,l}^{LH}$, for all the given values of l ; (b): the temperature pattern on Γ_M when the cavity is given by $\Gamma_{C,l}^{LV}$, for all given values of l ; (c): the temperature pattern on Γ_M when the cavity is given by $\Gamma_{C,l}^{LH}$, for all given values of l ; (d): the computed least value for each of the measured temperatures shown in (b) and (c).

of the exact cavities:

$$\Gamma_C^{LN} = \left\{ \begin{pmatrix} 0.6 \cos t \\ 0.4 + 0.3 \sin t \end{pmatrix}, t \in [0, 2\pi) \right\}, \quad \Gamma_C^{LF} = \left\{ \begin{pmatrix} 0.6 \cos t \\ -0.4 + 0.3 \sin t \end{pmatrix}, t \in [0, 2\pi) \right\},$$

for the first two test cases, and

$$\Gamma_C^{SN} = \left\{ \begin{pmatrix} 0.4 + 0.2 \cos t \\ 0.4 + 0.1 \sin t \end{pmatrix}, t \in [0, 2\pi) \right\}, \quad \Gamma_C^{SF} = \left\{ \begin{pmatrix} -0.4 + 0.2 \cos t \\ -0.4 + 0.1 \sin t \end{pmatrix}, t \in [0, 2\pi) \right\},$$

for the last two situations. The temperature patterns for the first two test cases are shown in Figure 4a and Figure 4b while the temperature pattern for the last two test cases are depicted in Figure 5a and Figure 5b. We initialize the geometry of the cavity base on these thermal patterns. Moreover, by taking into account the idea built from the discussion issued in the previous example, we terminate the algorithm with $\theta = 10^{-3}$ for cases with large cavities and set $\theta = 10^{-4}$ for cases where only a relatively small cavity is expected in the interior of the specimen.

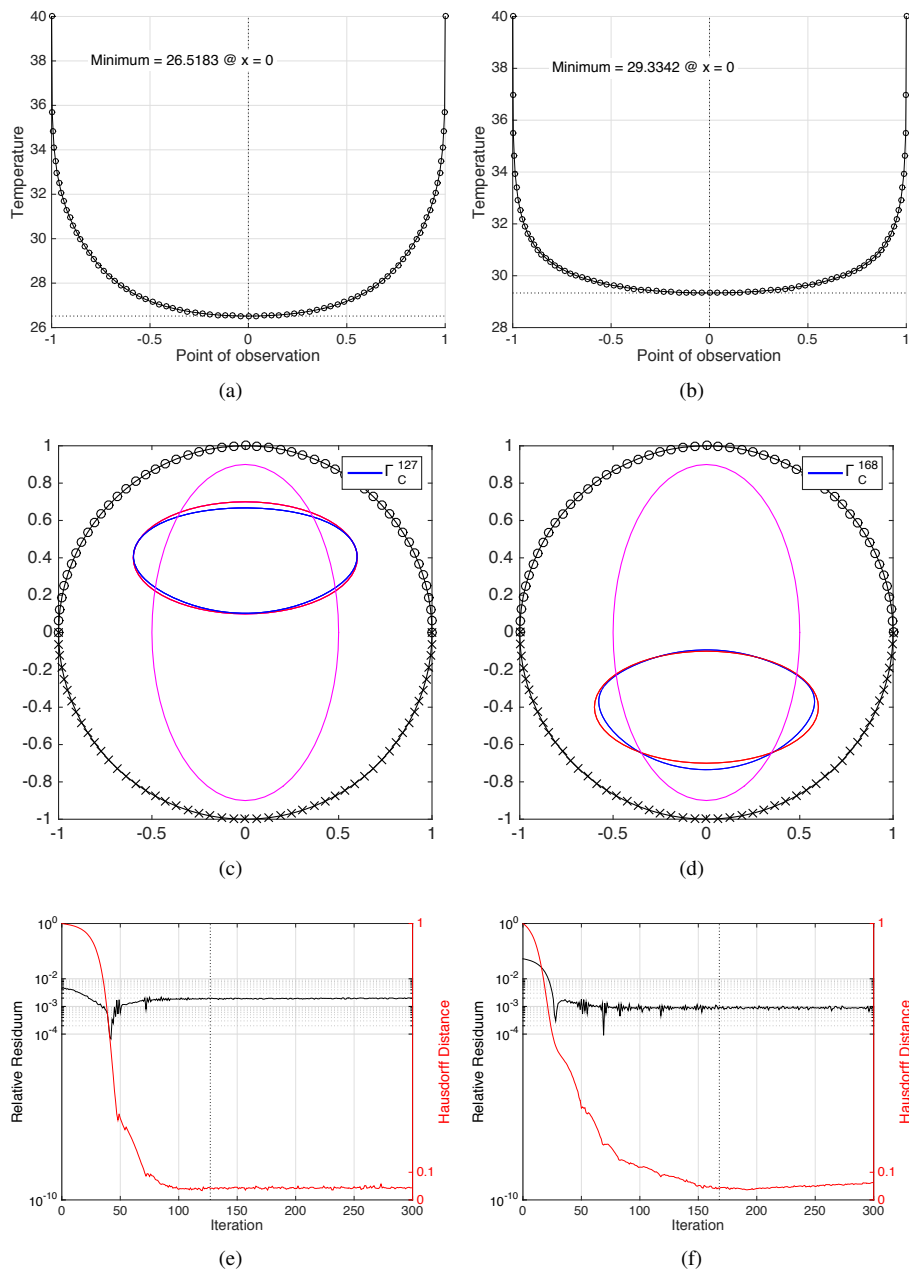


Fig. 4: (a)-(b): Respective temperature patterns on Γ_M for the elliptical cavities Γ_C^{LN} and Γ_C^{LF} ; (c)-(d): respective results of the identifications of the elliptical cavities Γ_C^{LN} and Γ_C^{LF} ; (e)-(f): respective histories of relative residuums and histories of Hausdorff distances for the test results depicted in (c) and (d).

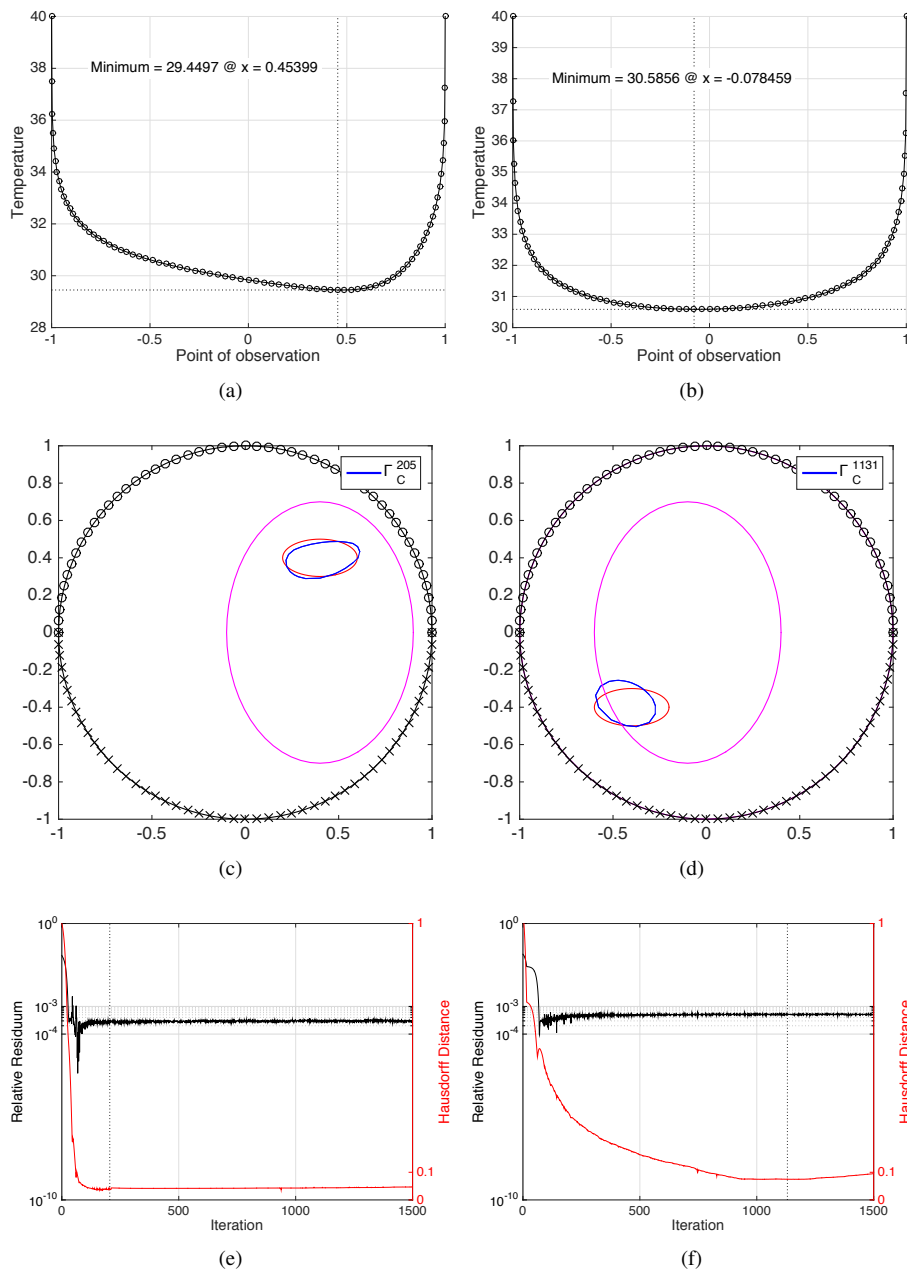


Fig. 5: (a)-(b): Respective temperature patterns on Γ_M for the elliptical cavities Γ_C^{SN} and Γ_C^{SF} ; (c)-(d): respective results of the identifications of the elliptical cavities Γ_C^{SN} and Γ_C^{SF} ; (e)-(f): respective histories of relative residuums and histories of Hausdorff distances for the test results depicted in (c) and (d).

Remark 2 As pointed out earlier, the value of θ is decided depending on the size of the expected cavity. To overcome the difficulty in estimating the size of the defect when it is situated far from the region of measurement, we can perform several boundary measurements, changing the region where measurement is made, and then examine the resulting temperature patterns. In this way, we can possibly obtain a plot for the temperature profile that has a pointed vertex, and then infer from it the size of the cavity. However, this idea only works well when the entire surface of the specimen (or at least a large part of it) is accessible for measurement. In all of the remaining test cases we consider here, although we only use a single boundary measurement to carry out the iterative procedure, we suppose that additional boundary measurements were performed to decide the value of θ .

For large cavities Γ_C^{LN} and Γ_C^{LF} , the stopping criterion is met after 127 and 168 iterations, respectively. The respective computed cavities for these two cases are shown in Figure 4c and Figure 4d. In both situations, we obtain reasonable identifications of the cavities regardless of its location.

On the other hand, for small cavities Γ_C^{SN} and Γ_C^{SF} , near and far from the region of measurement, the stopping criterion is met after 205 and 1131 iterations, respectively. The respective reconstructed cavities for these two cases are depicted in Figure 5c and Figure 5d. As one can observe, the identification process gives better result for the test case wherein the cavity is near the region of measurement. The result for the other case, however, is still acceptable as we have obtained a good location of the exact cavity.

Meanwhile, referring to the last two plots in Figure 4 and Figure 5, we observe that for cavities near the region of measurement, the Hausdorff distance at each iterative step remains below a certain value after some number of iterations (see, in particular, Figure 4e and Figure 5e). In contrary, for cases where cavities are far from the boundary where measurements are performed, the computed Hausdorff distance increases a bit after a certain number of iterations is reached (refer to Figure 4f and Figure 5f). We believe this come from the inherent ill-posedness of the inverse problem and could also be due to the ill-posedness of the shape optimization formulation. Further, we remark that these latter plots indicate that the computed shapes are the best reconstruction we can obtain from the identification process (i.e., the approximations can no longer be improved even we go beyond 168 and 1131 iterations for the case of Γ_C^{LF} and Γ_C^{SF} , respectively).

5.3 Third case: identification of cavities with noised synthetic data

Next, we test the effectiveness of the identification process for cases wherein the synthetic data is contaminated with some level of noise. Here, we stress that the least-squares formulation of the cavity identification problem is ill-posed; that is, arbitrarily small perturbations in the measurements may result into arbitrarily large differences in the identified cavities. Hence, we only perform some tests with small noise levels (e.g., $\gamma = 1\%, 3\%$). We consider the same geometries of the cavities given in the second test case. The thermal patterns in the case when the defect is described by Γ_C^{LN} , Γ_C^{LF} , Γ_C^{SN} , Γ_C^{SF} , with synthetic data under noise levels $\gamma = 1\%, 3\%$, are shown in Figure 6a, Figure 6b, Figure 7a and Figure 7b, respectively. In view of these aforementioned figures, we notice that it is quite difficult to determine which observation point has the least temperature value. To succeed in dealing with this problem, we apply several polynomial interpolations (with odd degree) on the set of thermal measurements on the observable boundary Γ_M and then find the mean location from the set of minimum values computed from these interpolations. For each of the present test cases, the

estimated mean location where the least temperature occurs is marked by a vertical line in the previously mentioned figures. Again, we initialize the geometry of the cavity base on these observations and we stop the algorithm under the same conditions specified in the previous test case. The results of the reconstructions under noise levels $\gamma = 1\%, 3\%$ are shown in Figure 6c, Figure 6d, Figure 7c and Figure 7d, where the number of iterations are also indicated. Notice that even at the given noise levels we are still able to obtain reasonable identifications of the cavities. Note that these approximations cannot be further improve based on Figures 6e, Figures 6f, Figures 7e and Figures 7f; that is, the data does not provide more information to get better identifications, since the cost values are already in the magnitude of the noise levels.

5.4 Fourth case: identification of cavities with non-trivial shapes

As we saw from the previous test cases, the identification process seems to be effective to reconstruct cavities having ‘simple shapes’. Now, we aim to identify cavities that have non-trivial shapes. More precisely, we want to detect a triangular-like shape cavity with rounded corners Γ_C^Δ (with small concavities) and a kite shape cavity Γ_C^K respectively represented by

$$\Gamma_C^\Delta = \left\{ \begin{pmatrix} -0.5 + 0.25 \cos t + 0.15 \cos 2t \\ 0.35 \sin t \end{pmatrix}, t \in [0, 2\pi) \right\},$$

$$\Gamma_C^K = \left\{ 0.6(1 + 0.15 \cos(3t + \pi/2)) \begin{pmatrix} \cos t \\ \sin t \end{pmatrix}, t \in [0, 2\pi) \right\}.$$

The thermal patterns measured on the boundary Γ_M when the cavity is described by Γ_C^Δ and Γ_C^K are shown in Figure 8a and Figure 8b, respectively. Using these measurements we initialize the geometry of the cavities as depicted in Figure 8c and Figure 8d, and use the value $\theta = 10^{-3}$ in our stopping condition (39). The identified shapes are also shown in the latter two figures where the number of iterations for each of the test cases (with 1% and 3% noised data) are indicated. Looking at the identified shapes for Γ_C^Δ and Γ_C^K , we see reasonable reconstructions of the target geometries for the given cavities. Moreover, we observe the non-convexity of the approximate shapes even for a noise level of 3%, and, in addition, the algorithm predicts at least positive and negative curvatures at the correct positions (at least on parts of the defect near the region of measurement). Again, since the reconstructed cavities results in values of the objective function in the magnitude of the noise levels (refer to Figure 8e and Figure 8f), we cannot expect to get better results with the noisy data.

Remark 3 (Some comments on the choice of θ) In the previous test cases, the reason behind the choice of θ is that when θ is set to 10^{-4} instead of 10^{-3} in cases when the specimen contains a large defect, we obtain a more ‘flat’ reconstruction of the unknown cavity. This result could be due to the instability of the shape optimization formulation of the inverse problem which is evident, for instance, from the history of the Hausdorff distances plotted in Figure 6f and Figure 8e.

Remark 4 (Some remarks on the value of the penalization parameter) We mentioned in the previous section that we choose the penalization parameter β by trial and error. In above test cases, β is taken in the interval $(0, 1]$. Testing several values of β , we notice that when it is set too small, the interior boundary of Ω (representing the surface of the cavity) becomes too rough or ‘jagged’ after several iterations, causing a problem in the remeshing process. On the other hand, taking β too big causes the reconstructed boundary to become too ‘flat’.

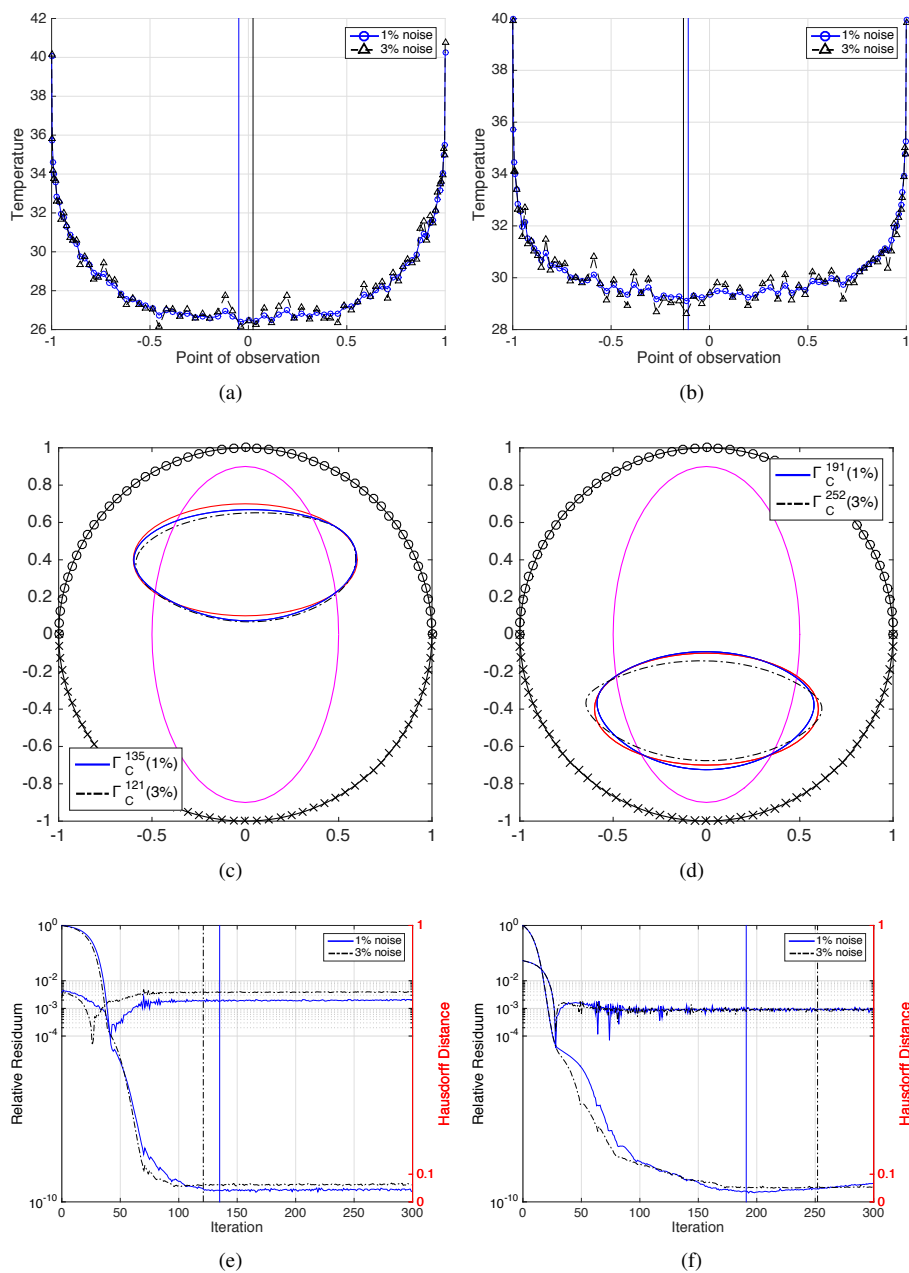


Fig. 6: (a)-(b): Respective temperature patterns on Γ_M when the defect is described by the elliptical cavities $\Gamma_C^{LN}(\gamma)$ and $\Gamma_C^{LF}(\gamma)$ with synthetic data under noise levels $\gamma = 1\%, 3\%$; (c)-(d): respective results of the identifications of the elliptical cavities $\Gamma_C^{LN}(\gamma)$ and $\Gamma_C^{LF}(\gamma)$ when the synthetic data is prescribed with noise levels $\gamma = 1\%, 3\%$; (e)-(f): respective histories of relative residuums and histories of Hausdorff distances for the test results depicted in (c) and (d).

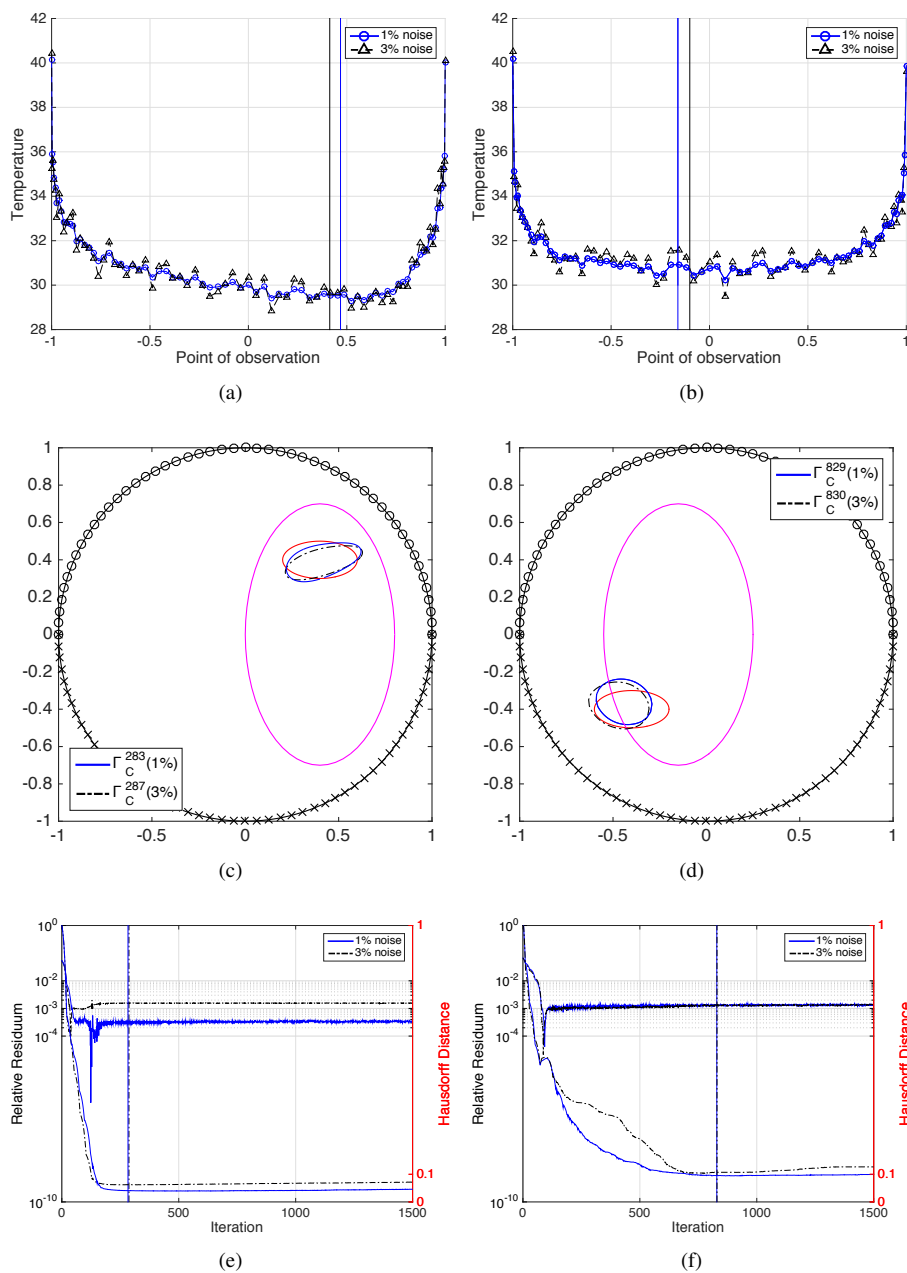


Fig. 7: (a)-(b): Respective temperature patterns on Γ_M when the defect is described by the elliptical cavities $\Gamma_C^{SN}(\gamma)$ and $\Gamma_C^{SF}(\gamma)$ with synthetic data under noise levels $\gamma = 1\%, 3\%$; (c)-(d): respective computed shapes of the elliptical cavities $\Gamma_C^{SN}(\gamma)$ and $\Gamma_C^{SF}(\gamma)$ when the synthetic data is prescribed with noise levels $\gamma = 1\%, 3\%$; (e)-(f): respective histories of relative residuums and histories of Hausdorff distances for the test results depicted in (c) and (d).

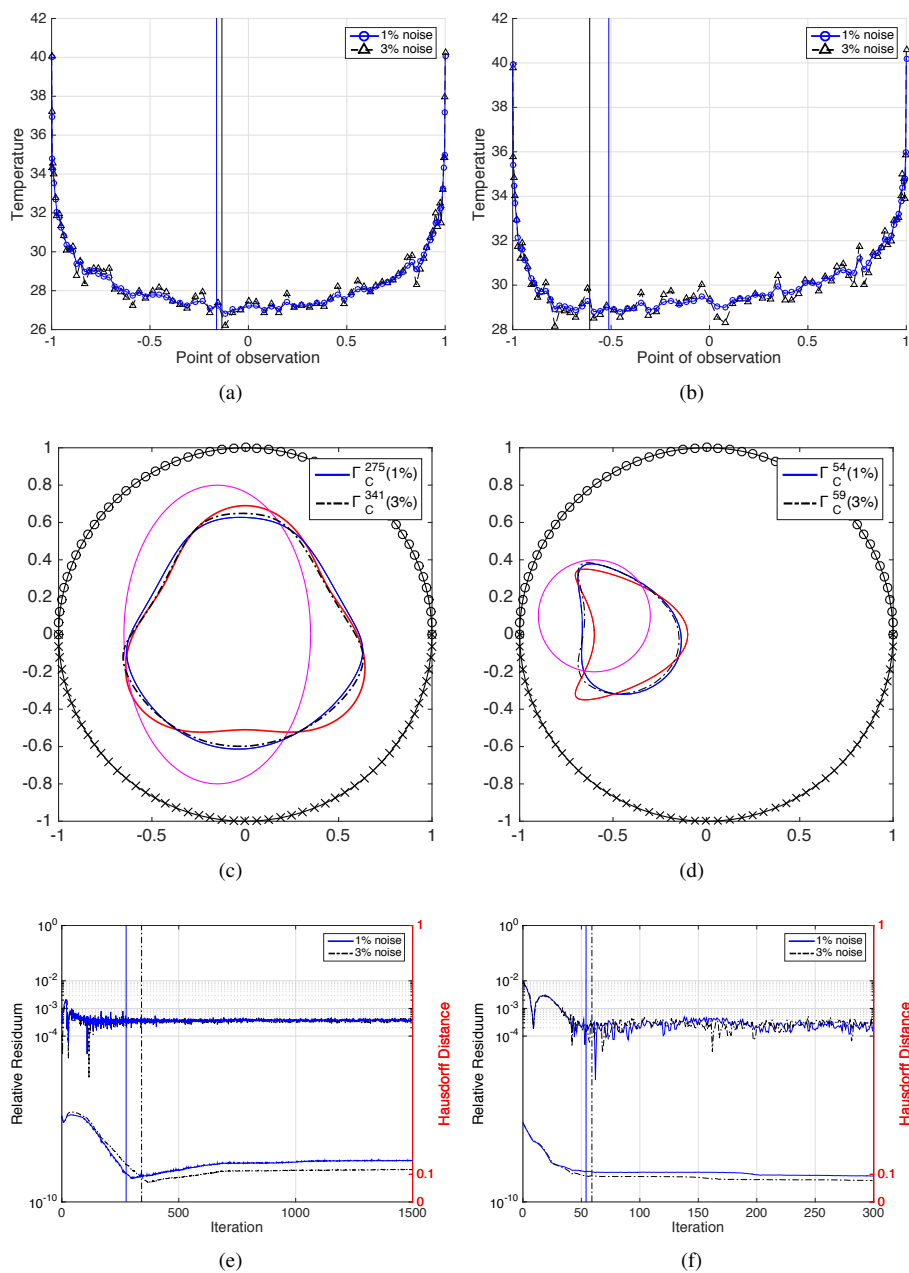


Fig. 8: (a)-(b): Respective temperature patterns on Γ_M when the defect is described by the triangular-shaped cavity $\Gamma_C^{\Delta}(\gamma)$ and kite-shaped cavity $\Gamma_C^K(\gamma)$ with synthetic data under noise levels $\gamma = 1\%, 3\%$; (c)-(d): respective identified shapes for the cavities $\Gamma_C^{\Delta}(\gamma)$ and $\Gamma_C^K(\gamma)$ when the synthetic data is prescribed with noise levels $\gamma = 1\%, 3\%$; (e)-(f): respective histories of relative residuums and histories of Hausdorff distances for the test results depicted in (c) and (d).

Remark 5 (A comment about the above inverse analyses) As is known, the inverse problems, such as the ones being considered here, are inherently lacking in information. Hence, additional information is necessary to conduct the inverse analyses. In the test cases examined above, the temperature output on Γ_M was used as primary information to conduct the inverse analyses. In addition, a priori information such as the knowledge based on experience about the influence of the location of the cavity on the thermal pattern observed on Γ_M was effectively used to improve the result of the inverse process. This kind of information is called *secondary* or *subsidiary* information as stated by Kubo in [37], and in actuality, such use of priori knowledge is recommended by experts in the field.

5.5 Fifth case: influence of the input data

As for our last test case for the cavity identification problem, we want to examine the influence of the input data on the resulting identifications. To address this objective, we shall consider two different scenarios where we have a large difference between the prescribed temperature on the edges and midsection of the specimen. More precisely, we examine the effect of the following prescribe temperature values

$$u_{P1} = 40(1.5 + 0.5 \cos 2x), \quad u_{P2} = 40(1.5 - 0.5 \cos 2x),$$

on the resulting identified shapes. The geometries of the cavities are again given by Γ_C^Δ and Γ_C^K . The computed thermal patterns for the two scenarios with prescribed temperatures $u_P = u_{P1}, u_{P2}$ (and also $u_P = u_{P0} = 40^\circ\text{C}$ for comparison) are shown in Figure 9a and Figure 9b, respectively. We notice that even under the prescribed temperatures we are able to identify which section of the specimen the cavity might be located. So, we initialize the geometry of the cavity based on these informations and terminate the iteration process with $\theta = 10^{-3}$. The reconstructed boundaries for the present test cases are depicted in Figure 9c and Figure 9d, respectively. As one can observe from the aforementioned figures, the reconstruction is much worse in the case of identifying Γ_C^Δ . On the other hand, we obtain a reasonable reconstruction for Γ_C^K as evident in Figure 9d. Similar to the previous test cases, the algorithm still predicts positive and negative curvatures at the correct positions, at least on parts of the cavity near the region of measurement. Meanwhile, the histories of the relative residuums and Hausdorff distances for these test cases are shown in Figure 9e and Figure 9f. Based on these results, it turns out that prescribing higher temperature values on the midsection of the specimen is much more practical and produces better results compared to prescribing higher temperature values on the edges of the specimen. We believe that this holds because in the midsection of the specimen occurs the largest distance between the region where heat is prescribed and the surface where measurement is performed. It seems that, in our case, and more likely in general, it is much reasonable to prescribe a uniform heat on the (bottom) surface of the specimen to obtain the best possible and more stable reconstructions. Nevertheless, we believe that even more research is required in order to fully understand the influence of the input data on the resulting reconstructions.

5.6 Numerical experiments for the corrosion detection problem

Here we provide some numerical results for the case of corrosion detection. The iterative algorithm is essentially the same with the one used for the cavity identification problem.

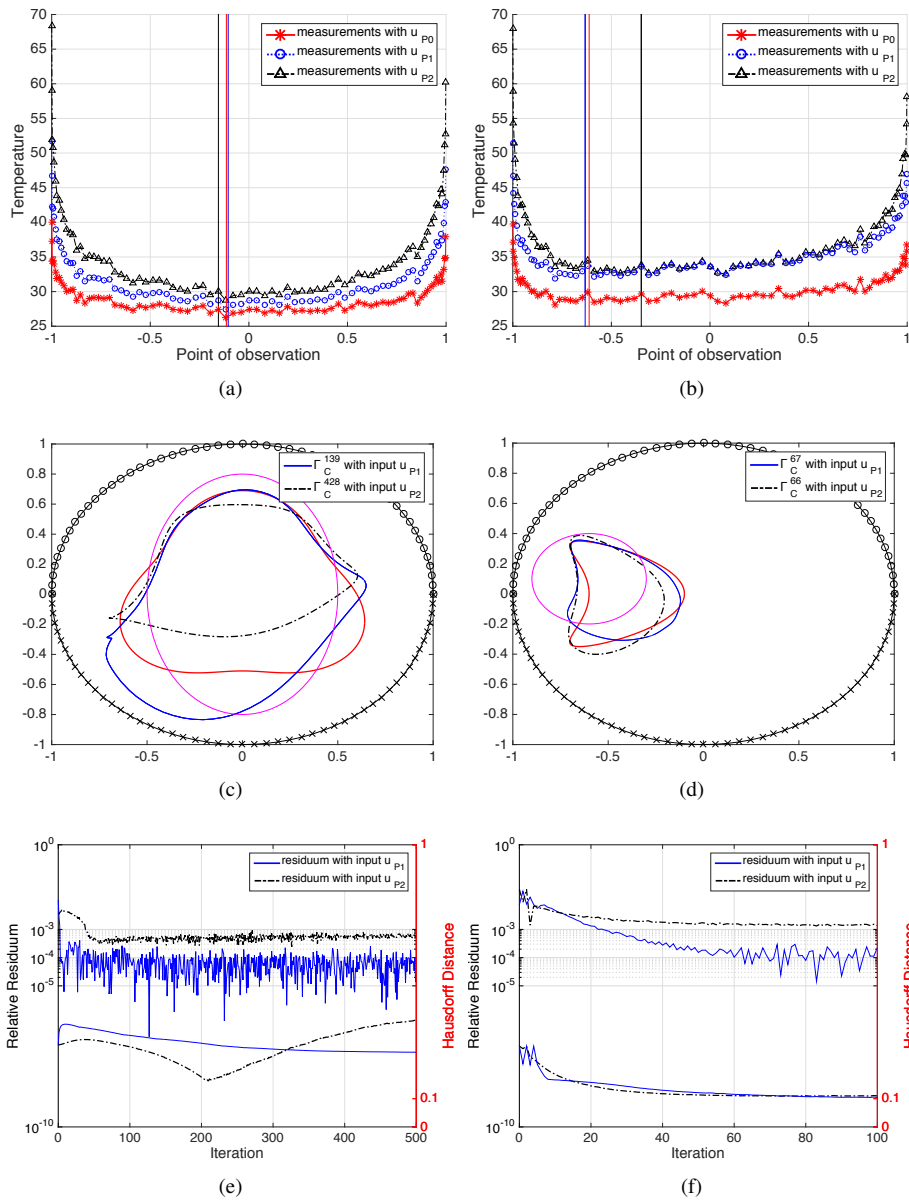


Fig. 9: (a)-(b): Temperature patterns on Γ_M when the cavity is described by $\Gamma_C^\Delta(\gamma)$ and $\Gamma_C^K(\gamma)$, respectively, with synthetic data under the noise level $\gamma = 3\%$ for various input data $u_P = u_{P0}, u_{P1}, u_{P2}$; (c)-(d): respective identified shapes for the cavities $\Gamma_C^\Delta(\gamma)$ and $\Gamma_C^K(\gamma)$; (e)-(f): respective histories of relative residuums and histories of Hausdorff distances for the test cases depicted in (c) and (d).

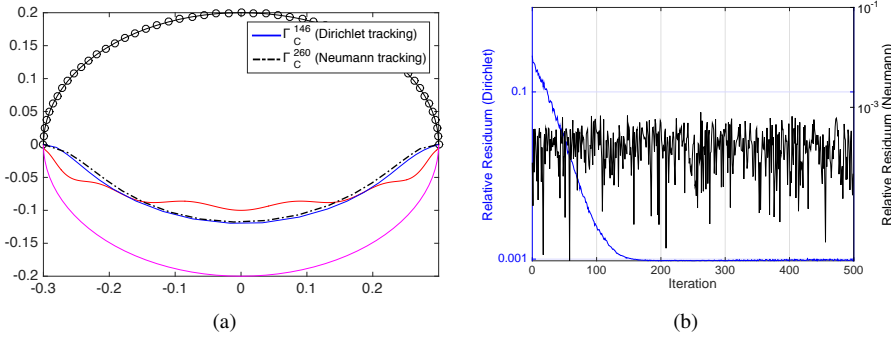


Fig. 10: (a): Reconstructions of Γ_C^1 for $\lambda = 10$ with 3% noisy data by tracking the Dirichlet data and tracking the Neumann data; *black line with circle marker*: Γ ; *red line*: Γ_C^1 ; *magenta line*: Γ_C^0 ; (b): histories of relative residuums for the case of tracking the Dirichlet data and tracking the Neumann data.

As in the previous section, we can generate the synthetic data by solving the forward problem (3) for the case of tracking the Neumann data and system (30) to the case of tracking the Dirichlet data. However, in both of the optimization problems (5) and (31), we shall only use system (30) to generate the synthetic data with $g = 2$. Nevertheless, we can resolve (3) by taking f as $u|_{\Gamma}$ obtained from solving the PDE system (30). We shall examine the accuracy of the two shape optimization formulations by looking at the relative residuums computed using the ratio $\|u - f\|_{L^2(\Gamma)} / \|f\|_{L^2(\Gamma)}$. Also, similar to the case of cavity identification, we use a different number of discretization points with higher polynomial degree for the finite element basis functions when generating the Cauchy pair (f, g) than the inversion process (Step 2 of the algorithm) to again avoid inverse crimes. Moreover, the stopping time for the iterative process is again dictated by the inequality condition (39). In all test cases we consider below, we set $\theta = 10^{-4}$. Furthermore, for simplicity, we assume that the corroded part of the object can again be represented in polar coordinates.

We begin by presenting numerical examples with $\lambda = 10$. First, we assume that the observable boundary Γ and the exact geometry of the corroded part Γ_C^1 of $\partial\Omega$ are respectively described as

$$\Gamma = \left\{ \begin{pmatrix} 0.3 \cos t \\ 0.2 \sin t \end{pmatrix}, t \in [0, \pi) \right\}, \quad \Gamma_C^1 = \left\{ \begin{pmatrix} 0.3 \cos t \\ 0.1 \sin t + 0.01 \sin^2 6t \end{pmatrix}, t \in [\pi, 2\pi) \right\}.$$

We start the iteration process with Γ_C^0 as the initial guess for Γ_C^1 , where

$$\Gamma_C^0 = \left\{ \begin{pmatrix} 0.3 \cos t \\ 0.2 \sin t \end{pmatrix}, t \in [\pi, 2\pi) \right\}.$$

The reconstructed corroded part of $\partial\Omega$ using $\mathcal{J}_D(\Gamma_C)$ and $\mathcal{J}_N(\Gamma_C)$ for 3% Gaussian noise added to the synthetic data are shown in Figure 10a. In both cases, the reconstruction process results in values of the objective function in the magnitude of the noise levels as depicted in Figure 10b. Hence, the results obtained were the best reconstruction we can get from the noisy data.

Influence of the number of oscillations on the unknown boundary and effect of the value of λ . We examine the influence of the number of oscillations on the unknown boundary

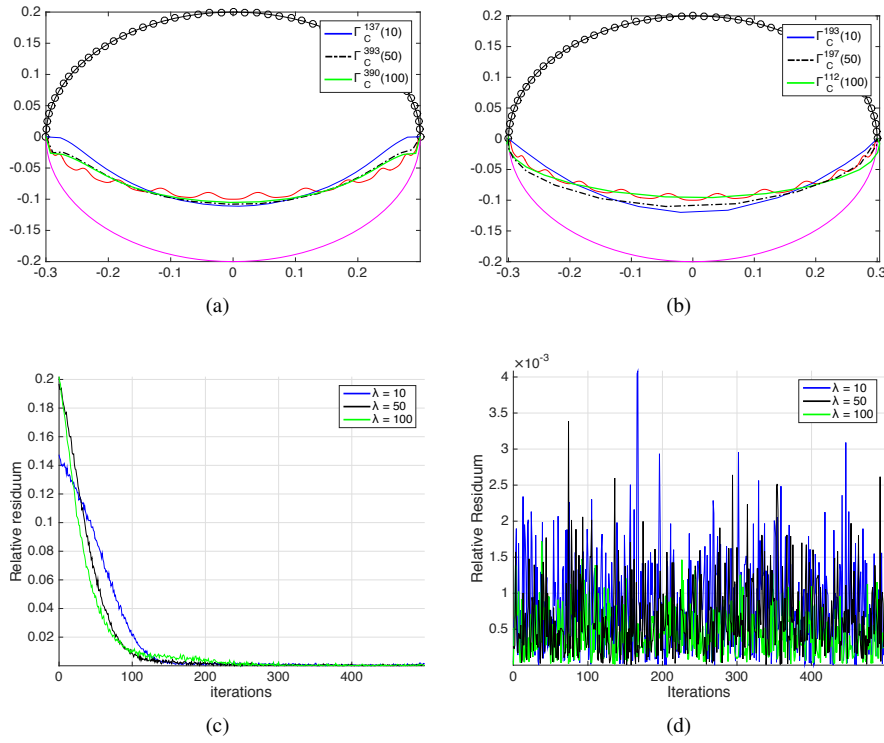


Fig. 11: (a) Reconstructions of $\Gamma_C^2(\lambda)$, for $\lambda = 10, 50, 100$, with 3% noisy data in the case of tracking the Dirichlet data; (b) reconstruction of $\Gamma_C^2(\lambda)$, for $\lambda = 10, 50, 100$, with 3% noisy data in the case of tracking the Neumann data; (c) histories of relative residuums, under the different values of λ , for the case of tracking the Dirichlet data shown in (a); (d) histories of relative residuums, under the different values of λ , for the case of tracking the Neumann data shown in (b).

as well as the effect of the value of λ on the reconstructed boundary. For this purpose, we consider the following geometry for the unknown boundary of $\partial\Omega$:

$$\Gamma_C^2 = \left\{ \begin{pmatrix} 0.3 \cos t \\ 0.1 \sin t + 0.01 \sin^4 12t \end{pmatrix}, t \in [0, \pi) \right\}.$$

The boundaries Γ and Γ_C^0 are the same with the previous example. The result of the reconstruction process under 3% noisy data, with values $\lambda = 10, 50, 100$, are shown in Figure 11a for the case of tracking the Dirichlet data. Meanwhile, Figure 11b shows the reconstructed boundaries for the same values of λ , again with 3% noisy data, but for the case of tracking the Neumann data. We observe that the number of oscillations on the corroded part does not much affect the result of the reconstruction process. The histories of the relative residuums for each of the test cases under the two formulations are shown in Figure 11c and Figure 11d, respectively. Clearly, the values of the cost functions are already below the magnitude of the noise level, so, the reconstructions cannot be further improved under the noisy data.

Reconstruction of the lower half of a kite-shape object. We examine a few more examples with the following descriptions for the accessible and exact geometry of the unknown

boundary:

$$\Gamma = \left\{ \begin{pmatrix} 0.3 \cos t + 0.1 \cos 2t \\ 0.2 \sin t \end{pmatrix}, t \in [0, \pi) \right\}, \quad \Gamma_C^3 = \left\{ \begin{pmatrix} 0.3 \cos t + 0.1 \cos 2t \\ 0.3 \sin t + 0.01 \sin^4 12t \end{pmatrix}, t \in [\pi, 2\pi) \right\}.$$

For the initial guess we set Γ_C^0 as

$$\Gamma_C^0 = \left\{ \begin{pmatrix} 0.1 + 0.3 \cos t \\ 0.45 \sin t \end{pmatrix}, t \in [\pi, 2\pi) \right\}.$$

The reconstructed boundaries for the case of Dirichlet-tracking formulations are shown in Figure 13a when $\lambda = 10, 50, 100$. Meanwhile, under the same situations, but for the case of tracking the Neumann data, the results are shown in Figure 13b. Again, as depicted in Figure 13c and Figure 13d, the reconstructions result in values of the objective function in the magnitude of the noise levels. Hence, the results shown in Figure 13a and Figure 13b are the best reconstructions we can get from the noisy data.

Influence of the initial guess. For our final test case, we examine the influence of the initial guess to the resulting reconstructions. In this regard, we consider the following initial profile of Γ_C :

$$\Gamma_C^{0\text{new}} = \left\{ \begin{pmatrix} 0.1 + 0.3 \text{sign}(\cos t) \sqrt{|\cos t|} \\ 0.4 \text{sign}(\sin t) \sqrt{|\sin t|} \end{pmatrix}, t \in [\pi, 2\pi) \right\},$$

where $\text{sign}(\cdot)$ denotes the signum function. The results of the reconstructions are depicted in Figure 13a and Figure 13b for the case of tracking the Dirichlet data and tracking the Neumann data, respectively. The corresponding history of relative residuums for the two formulations are shown in Figure 13c and Figure 13d, respectively. We notice that the choice of initial guess does not have much effect on the result of the reconstructions (except, of course, on the number of iterations) when using the tracking Dirichlet data functional. However, a slight difference of results can be observed when the tracking Neumann data functional is used. In fact, with the new initial guess $\Gamma_C^{0\text{new}}$, the reconstructions were somehow improved based on the relative residuum shown in Figure 13d. Nevertheless, the reconstructed boundaries for both of the test cases are reasonable under the given noise.

Remark 6 In above examples, we tested several values for β and we observed that it suffices to take β from the interval $[0.0001, 0.01]$ when the cost functional $\mathcal{J}_D(\Gamma_C)$ is used. Meanwhile, for cases where the cost functional $\mathcal{J}_N(\Gamma_C)$ is being utilized, β has to be chosen from the interval $[1, 10]$ depending on the value of λ . We stress that this high value of the penalization parameter β might be an indication of the ill-posedness of the least-squares cost functional $\mathcal{J}_N(\Gamma_C)$. We notice that when β is taken much higher compared to these aforementioned values, the iteration process becomes unstable and Ω becomes too flat (i.e., degenerates in shape) after several iterations. On the other hand, when β is set too small, the rate of convergence of the iteration process becomes insignificant.

Summarizing, the numerical experiments show rather satisfying reconstructions for larger values of λ . It appears that for smaller values of λ the reconstructions start to deteriorate which, as pointed out in [18], could be due to the way the synthetic data were created since for small λ we get close to the not uniquely solvable Neumann problem.

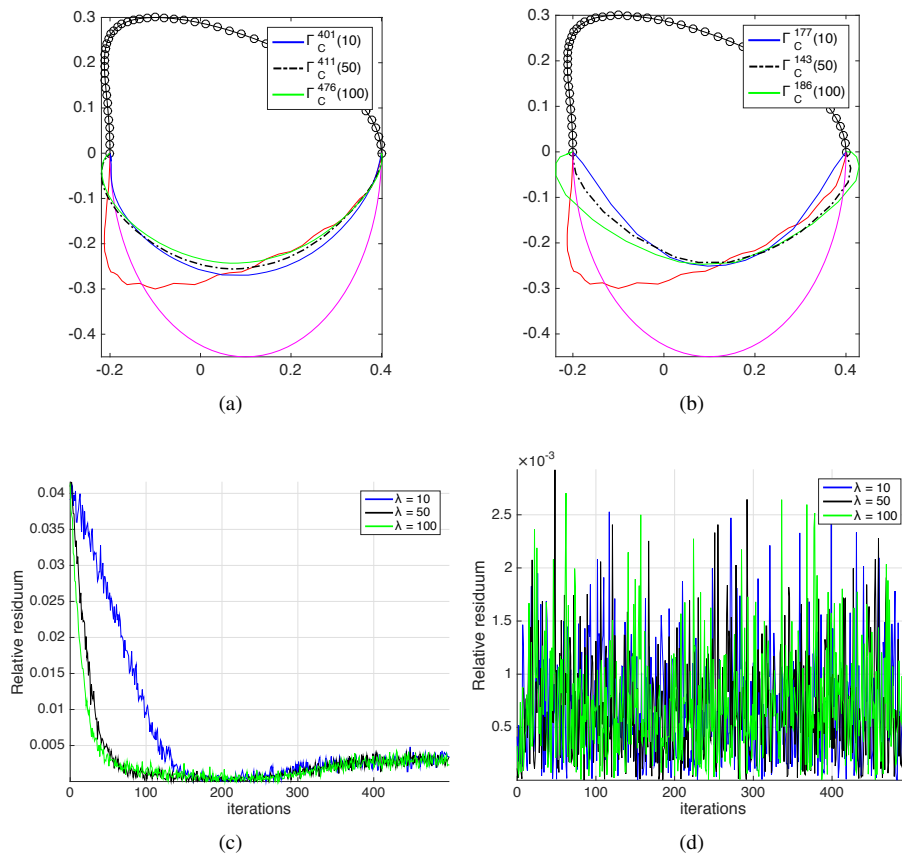


Fig. 12: (a) Reconstructions of $\Gamma_C^3(\lambda)$, for $\lambda = 10, 50, 100$, with 3% noisy data in the case of tracking the Dirichlet data; (b) reconstruction of Γ_C^3 , for $\lambda = 10, 50, 100$, with 3% noisy data in the case of tracking the Neumann data; (c) histories of relative residuums, under different values of λ , for the case of tracking the Dirichlet data shown in (a); (d) histories of relative residuums, under different values of λ , for the case of tracking the Neumann data shown in (b).

6 Summary, Conclusion and Recommendations

We have obtained fair reconstructions of a defect by minimizing a least-squares functional using partial boundary measurements inspired by the concept of non-destructive testing and evaluation. In the focused problem, the object was assumed to be a heat-conducting medium having an interior cavity with convective boundary condition and the problem was examined under the notion of thermal imaging. In addition, the case where the defect appears on a part of the surface of the specimen was also considered. The inverse problem was interpreted in the context of corrosion detection where the reconstruction of the impenetrable boundary was carried out using partial (electrostatic) Cauchy data. The respective solutions to these geometric inverse problems were sought through the methods of shape optimization using Dirichlet-data-tracking functionals, and also by tracking the Neumann data on the

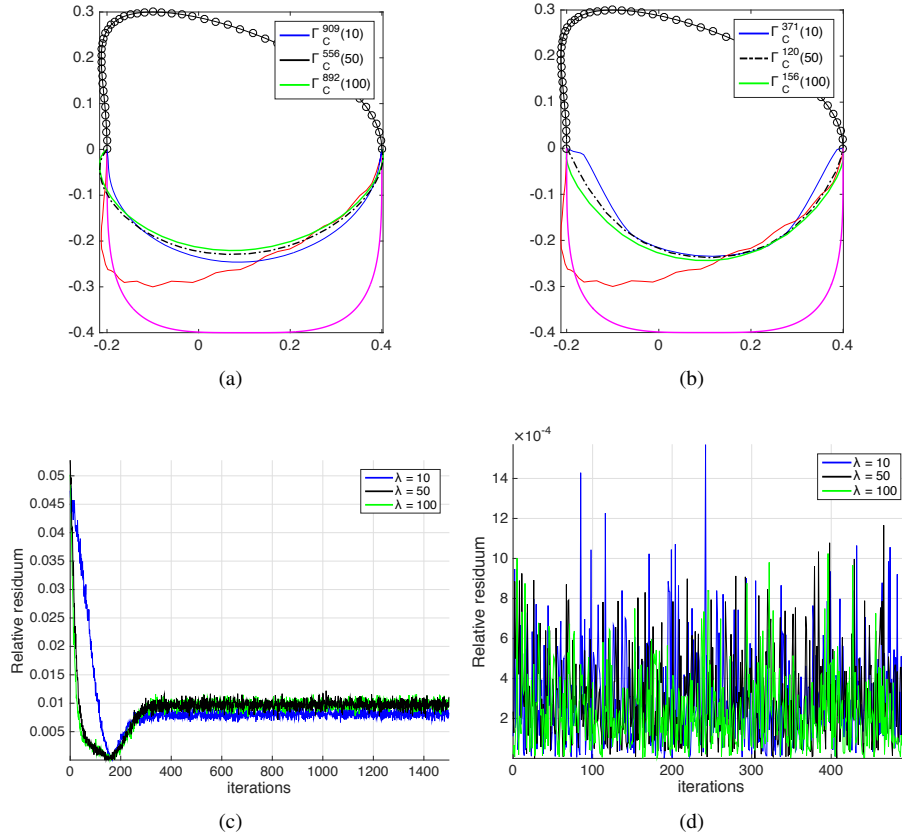


Fig. 13: (a) Reconstructions of Γ_C^3 with initial guess Γ_C^{0new} with $\lambda = 10, 50, 100$ under 3% noisy data for the tracking the Dirichlet data; (b) reconstruction of Γ_C^3 with initial guess Γ_C^{0new} with $\lambda = 10, 50, 100$ under 3% noisy data for the tracking the Neumann data; (c) histories of relative residuums, under different values of λ , for the case of tracking the Dirichlet data shown in (a); (d) histories of relative residuums, under different values of λ , for the case of tracking the Neumann data shown in (b).

accessible part of the boundary for the case of corrosion detection. The computation of the first-order shape derivative of the cost functionals were carried out through minimax formulation, employing the function space parametrization technique and an important theorem due to Correa and Seeger [21] for the differentiation of the min-max functional. Then, using the computed boundary expression for the shape gradients, we were able to formulate and successfully implemented a boundary variation scheme for the numerical realization of the shape optimization problems. The proposed identification procedure produced reasonable reconstructions of the unknown boundaries even at 3% noisy data.

The investigations delivered in this paper still leave space for further studies towards several directions. First, we only considered objects having a single cavity which might not be the case in most real situations. In fact, in reality, we do not know whether a given specimen contains only a single cavity. Nevertheless, for situations such as the ones examined in this present investigation, a numerical scheme based on a Lagrangian approach is enough

to identify the geometry of the unknown defect. For cases wherein more than one cavity is expected, an Eulerian approach such as the level-set method is more appropriate. Moreover, we note that the penalization perimeter was chosen by trial and error, and thus may not be optimal. Hence, it is also of interest to know how the penalization parameter can be decided analytically. The fully time-dependent case of the problem, as well as its extension to three-dimensional situations, will also make an interesting study. Furthermore, the computation of the deformation field was based on the H^1 gradient method, utilizing the computed expression for the shape gradient. It is also possible to formulate an H^1 Newton method to numerically solve the shape optimization problem which may improve the identification process. However, the numerical procedure for this method requires the knowledge of the second-order shape derivative of the cost functional which, as a consequence, may complicate the computation of the descent direction. Still, it would also be of interest to exhibit the expression for the shape Hessian of the cost functional and implement an iteration scheme using an H^1 Newton method to numerically solve the given geometric inverse problem.

7 Appendix

For completeness, we state here a theorem due to Correa and Seeger [21], which is key result for differentiating a minimax with respect to a parameter.

7.1 A theorem of Correa and Seeger

We first introduce some notations. Consider a functional

$$G : [0, \tau] \times X \times Y \rightarrow \mathbb{R},$$

for some $\tau > 0$ and topological spaces X and Y . For each t in $[0, \tau]$, we define

$$g(t) = \min_{x \in X} \sup_{y \in Y} G(t, x, y) \quad \text{and} \quad h(t) = \sup_{y \in Y} \min_{x \in X} G(t, x, y)$$

and the associated sets

$$X(t) = \left\{ \hat{x} \in X : \sup_{y \in Y} G(t, \hat{x}, y) = g(t) \right\} \quad \text{and} \quad Y(t) = \left\{ \hat{y} \in Y : \min_{x \in X} G(t, x, \hat{y}) = h(t) \right\}.$$

Given the above definitions, we introduce the *set of saddle points*

$$S(t) = \{(\hat{x}, \hat{y}) \in X \times Y : g(t) = G(t, \hat{x}, \hat{y}) = h(t)\},$$

which may be empty. In general, we always have the inequality $h(t) \leq g(t)$. Further, for a fixed t in $[0, \tau]$, and for all $(x^t, y^t) = (\hat{x}, \hat{y})$ in $X(t) \times Y(t)$, $h(t) \leq G(t, x^t, y^t) \leq g(t)$, and when $h(t) = g(t)$, the set of saddle points $S(t)$ is exactly $X(t) \times Y(t)$. Here, we are particularly interested on the situation when G admits saddle points for all t in $[0, \tau]$.

The objective of this method is to seek realistic conditions under which one can guarantee the existence of the limit

$$dg(0) = \lim_{t \searrow 0} \frac{g(t) - g(0)}{t}.$$

We now quote the improved version [22, Theorem 5.1, pp. 556–559] of the theorem of Correa and Seeger. The result also applies to situations when the state equation admits no unique solution and the Lagrangian admits saddle points. The proof of this theorem is also given in the said reference.

Theorem 1 ([21]) *Let the sets X and Y , the real number $\tau > 0$, and the functional*

$$G : [0, \tau] \times X \times Y \rightarrow \mathbb{R}$$

be given. Assume that the following assumptions hold:

- (H1) *for $0 \leq t \leq \tau$, the set $S(t)$ is non-empty;*
(H2) *for all $(x, y) \in [\cup\{X(t) : 0 \leq t \leq \tau\} \times Y(0)] \cup [X(0) \times \cup\{Y(t) : 0 \leq t \leq \tau\}]$, the partial derivative $\partial_t G(t, x, y)$ exists everywhere in $[0, \tau]$;*
(H3) *there exists a topology \mathcal{T}_X on X such that for any sequence $\{t_n : 0 < t_n \leq \tau\}$, $t_n \rightarrow t_0 = 0$, there exist an $x^0 \in X(0)$ and a subsequence $\{t_{n_k}\}$ of $\{t_n\}$, and for each $k \geq 1$, there exists $x_{n_k} \in X(t_{n_k})$ such that*
(i) *$x_{n_k} \rightarrow x^0$ in the \mathcal{T}_X -topology, and*
(ii) *for all y in $Y(0)$, the following inequality holds:*

$$\liminf_{\substack{t \searrow 0 \\ k \rightarrow \infty}} \partial_t G(t, x_{n_k}, y) \geq \partial_t G(0, x^0, y);$$

- (H4) *there exists a topology \mathcal{T}_Y on Y such that for any sequence $\{t_n : 0 < t_n \leq \tau\}$, $t_n \rightarrow t_0 = 0$, there exist $y^0 \in Y(0)$ and a subsequence $\{t_{n_k}\}$ of $\{t_n\}$, and for each $k \geq 1$, there exists $y_{n_k} \in Y(t_{n_k})$ such that*
(i) *$y_{n_k} \rightarrow y^0$ in the \mathcal{T}_Y -topology, and*
(ii) *for all x in $X(0)$, the following inequality holds:*

$$\limsup_{\substack{t \searrow 0 \\ k \rightarrow \infty}} \partial_t G(t, x, y_{n_k}) \leq \partial_t G(0, x, y^0).$$

Then, there exists $(x^0, y^0) \in X(0) \times Y(0)$ such that

$$dg(0) = \min_{x \in X(0)} \sup_{y \in Y(0)} \partial_t G(0, x, y) = \partial_t G(0, x^0, y^0) = \sup_{y \in Y(0)} \min_{x \in X(0)} \partial_t G(0, x, y).$$

Thus, (x^0, y^0) is a saddle point of $\partial_t G(0, x, y)$ on $X(0) \times Y(0)$.

7.2 Proof of Proposition 2: Verifications of assumptions (H1)–(H4)

In what follows, we formally prove Proposition 2 by verifying the four conditions of Theorem 1. As we have mentioned in passing, the arguments used in the proof follow the ideas issued in [22, Section 5.5] and are similar to [46, 47].

Verification of (H1). First, we show that $S(t) \neq \emptyset$. Let $\mathbf{V} \in \Theta_1$. In reference to [9, Lemma 6], we can find a sufficiently small number $\varepsilon > 0$, such that, for all $t \in [0, \varepsilon]$, there exists constants $\alpha_1, \alpha_2, \beta_1$ and β_2 satisfying $0 < \alpha_1 \leq \alpha_2, 0 < \beta_1 \leq \beta_2$ and such that

$$\alpha_1 |\xi|^2 \leq A_t \xi \cdot \xi \leq \alpha_2 |\xi|^2, \quad (40)$$

for all $\xi \in \mathbb{R}^2$ and

$$\beta_1 \leq w_t \leq \beta_2. \quad (41)$$

We define the following sets:

$$X(t) := \left\{ x^t \in H^1(\Omega) : \sup_{y \in W(\Omega)} \mathcal{G}(t, x^t, y) = \min_{x \in H^1(\Omega)} \sup_{y \in W(\Omega)} \mathcal{G}(t, x, y) \right\},$$

$$Y(t) := \left\{ y^t \in H^1(\Omega) : \min_{x \in H^1(\Omega)} \mathcal{G}(t, x, y^t) = \sup_{y \in W(\Omega)} \min_{x \in H^1(\Omega)} \mathcal{G}(t, x, y) \right\}.$$

The functions u^t and p^t satisfy the inequality $G(t, u^t, \psi) \leq G(t, u^t, p^t) \leq G(t, \varphi, p^t)$. Hence, it is evident that $X(t)$ and $Y(t)$ are non-empty, since, in particular, we have $X(t) = \{u^t\}$ and $Y(t) = \{p^t\}$. Thus, we have, for all $t \in [0, \varepsilon]$, $S(t) := X(t) \times Y(t) = \{(u^t, p^t)\} \neq \emptyset$. This verifies condition (H1).

Verification of (H2). Next, we compute the partial derivative $\partial_t \mathcal{G}(t, \varphi, \psi)$:

$$\begin{aligned} \partial_t \mathcal{G}(t, \varphi, \psi) &= \frac{1}{2} \int_{\Gamma_M} w'_t(\varphi - u_M) ds + \int_{\Omega} k A'_t \nabla \varphi \cdot \nabla \psi dx + \int_{\Gamma_P} w'_t(\varphi - u_P) \partial_n \psi ds \\ &\quad + \int_{\Gamma_M} w'_t [h_M(\varphi - u_\infty) - Q_M] \psi ds + \int_{\Gamma_C} w'_t [h_C(\varphi - u_C) - Q_C] \psi ds, \end{aligned}$$

where $A'_t = dA_t/dt$ and $A'_0 = \text{div} \mathbf{V} \mathbf{I}_2 - (D\mathbf{V} + (D\mathbf{V})^T)$. Since $\mathbf{V} \in \Theta_1$, then $t \mapsto DT_t$ is continuous in $[0, \varepsilon]$ (cf. [9, Lemma 11]). This implies that $\partial_t \mathcal{G}(t, \varphi, \psi)$ exists everywhere in $[0, \varepsilon]$. Hence, condition (H2) is also satisfied.

Verification of (H3) and (H4). To check the last two assumptions (H3) and (H4), we first show the boundedness of (u^t, p^t) . We only sketch the proof for the case of u^t , but we discuss in detail the case for p^t since the equations involved are simpler. The argument follows the same reasoning as in [22, Section 5.5, p. 560]. The idea is to take $\varphi = u^t$ (resp. $\varphi = p^t$) in equation (23) (resp. (24)) and use the boundedness of A_t and w_t given in (40) and (41), respectively. In the case of u^t , we need to prove that we can find a constant C_1 such that

$$\|u^t\|_{H^1(\Omega)}^2 \leq C_1 \left(\|\nabla u^t\|_{L^2(\Omega)}^2 + \|u^t\|_{L^2(\Gamma_M)}^2 + \|u^t\|_{L^2(\Gamma_P)}^2 + \|u^t\|_{L^2(\Gamma_C)}^2 \right).$$

Defining the norm $\|\cdot\|_\partial$ using the left-hand side of this inequality, one can show that it is actually equivalent to the usual H^1 -Sobolev norm $\|\cdot\|_{H^1(\Omega)}$, i.e., we can find constants c_1 and c_2 ($0 < c_1 \leq c_2$) such that

$$c_1 \|u^t\|_\partial \leq \|u^t\|_{H^1(\Omega)} \leq c_2 \|u^t\|_\partial. \quad (42)$$

To confirm the validity of the above claim, one can follow the line of arguments in the proof of Proposition 2 in [40]. The first inequality $c_1 \|u^t\|_\partial \leq \|u^t\|_{H^1(\Omega)}$ follows from the fact that the trace map $u^t \mapsto u^t|_{\partial\Omega}$ is a bounded linear operator (by Trace theorem). Meanwhile, the second inequality $\|u^t\|_{H^1(\Omega)} \leq c_2 \|u^t\|_\partial$ is shown by way of contradiction. The details of the proof is based on the validation of [40, Proposition 2] and is standard, so we omit it.

On the other hand, the proof for the boundedness of p^t in $W(\Omega)$ is laid out as follows. Firstly, we recall the definition of the norm on $W(\Omega)$ given by (6):

$$\|\varphi\|_{W(\Omega)}^2 = \|\nabla \varphi\|_{L^2(\Omega)}^2 + \|\varphi\|_{L^2(\Gamma_M)}^2 + \|\varphi\|_{L^2(\Gamma_C)}^2.$$

Taking $\varphi = p^t$ in equation (24) yields

$$\int_{\Omega} k A_t |\nabla p^t|^2 dx + \int_{\Gamma_M} h_M w_t (p^t)^2 ds + \int_{\Gamma_C} h_C w_t (p^t)^2 ds = \int_{\Gamma_M} w_t (u^t - u_M^t) p^t ds.$$

Hence, in view of (40), (41) and the fact that $T_t(x) = x$, $w_t = 1$ on Γ , together with the Cauchy-Schwarz inequality, we obtain

$$\begin{aligned} \min\{\beta_1 k, h_M, h_C \alpha_1\} \|p^t\|_{W(\Omega)}^2 &\leq \beta_1 k \int_{\Omega} |\nabla p^t|^2 dx + h_M \int_{\Gamma_M} w_t (p^t)^2 ds + h_C \int_{\Gamma_C} w_t (p^t)^2 ds \\ &\leq \|u^t\|_{L^2(\Gamma_M)} \|p^t\|_{L^2(\Gamma_M)} + |u_M|_{\infty} |\Gamma_M|^{\frac{1}{2}} \|p^t\|_{L^2(\Gamma_M)} \\ &\leq \left(c_4 \|u^t\|_{H^1(\Omega)} + |u_M|_{\infty} |\Gamma_M|^{\frac{1}{2}} \right) \|p^t\|_{W(\Omega)}, \end{aligned}$$

for some constant $c_4 > 0$. Therefore, since u^t is bounded in $H^1(\Omega)$, then we can conclude that p^t is bounded in $W(\Omega)$, i.e., there exists a constant $c > 0$ such that the inequality $\|p^t\|_{W(\Omega)} \leq c$ holds. This confirms the first part.

The next step is to show the continuity of the pair (u^t, p^t) . To prove the continuity of u^t , we subtract in (23) at $t > 0$, $t = 0$ and let $\varphi = u^t - u$. Hence, owing to the fact that $T_t(x) = x$ and $w_t = 1$ on Γ , we get

$$\begin{aligned} &\int_{\Omega} k \nabla(u^t - u) \cdot \nabla \varphi dx + \int_{\Gamma_C} h_C (u^t - u) \varphi ds \\ &= - \int_{\Omega} k (A_t - \mathbf{I}_2) \nabla u^t \cdot \nabla \varphi dx - \int_{\Gamma_C} h_C (w_t - 1) u^t \varphi ds + \int_{\Gamma_C} (w_t - 1) (h_C u_C - Q_C) \varphi ds, \end{aligned}$$

where $\varphi = u^t - u$. Utilizing the bound (41), and the equivalence of the norms $\|\cdot\|_{\partial}$ and $\|\cdot\|_{H^1(\Omega)}$, we know that there exists a constant $c_3 > 0$ such that

$$\begin{aligned} c_3 \|u^t - u\|_{H^1(\Omega)}^2 &\leq |k| \|A_t - \mathbf{I}_2\|_{L^\infty(\Omega)} \|\nabla u^t\|_{L^2(\Omega)} \|\nabla(u^t - u)\|_{L^2(\Omega)} \\ &\quad + |h_C| |\alpha_2 - 1| \|u^t\|_{L^2(\Gamma_C)} \|u^t - u\|_{L^2(\Gamma_C)} \\ &\quad + |\alpha_2 - 1| |h_C u_C - Q_C| |\Gamma_C|^{\frac{1}{2}} \|u^t - u\|_{L^2(\Gamma_C)}. \end{aligned}$$

Using the boundedness of u^t in $H^1(\Omega)$, the trace theorem, and the estimate (42), we get $\|u^t - u\|_{H^1(\Omega)} \leq c_5$, for some constant $c_5 > 0$. Furthermore, because of the strong continuity of A_t as a function of the parameter t , we infer that $u^t \rightarrow u$ in $H^1(\Omega)$ as $t \rightarrow 0$. By the same technique, we can prove the strong convergence $p^t \rightarrow p$ in $W(\Omega)$. So, conditions (H3)(i) and (H4)(i) are satisfied. Finally, assumptions (H3)(ii) and (H4)(ii) follows from the strong continuity of the maps $(t, \varphi) \mapsto \partial_t \mathcal{J}(t, \varphi, \psi)$ and $(t, \psi) \mapsto \partial_t \mathcal{J}(t, \varphi, \psi)$. Therefore, all assumptions of Theorem 1 are now satisfied. In concluding, the expression for the first-order shape derivative of $\mathcal{J}(\Gamma_C)$ along the velocity field \mathbf{V} over Ω is given by $d\mathcal{J}(\Gamma_C)[\mathbf{V}] = \partial_t \mathcal{J}(t, u, p)|_{t=0}$. This proves Proposition 2.

References

1. Afraites, L., Dambrine, M., Kateb D.: Shape methods for the transmission problem with a single measurement. *Numer. Funct. Anal. Optim.* **28**(5-6), 519–551 (2007)
2. Azegami, H.: A solution to domain optimization problems. *Trans of Japan Soc. of Mech. Eng.*, Ser A. **60**, 1479–1486 (1994) (in Japanese)
3. Azegami, H., Wu, Z.Q.: Domain optimization analysis in linear elastic problems: approach using traction method. *JSME Int. J.*, Ser. A **39**(2), 272–278 (1996)
4. Azegami, H., Kaizu, S., Shimoda, M., Katamine, E.: Irregularity of shape optimization problems and an improvement technique. in *Computer Aided Optimization Design of Structures V*, eds. Hernandez, S. and Brebbia, C. A.. Computational Mechanics Publications, Southampton, 309–326 (1997)

5. Azegami, H., Takeuchi, Z.: A smoothing method for shape optimization: traction method using the Robin condition. *Int. J. Comp. Meth-Sing.* **3**(1), 21–33 (2006)
6. Azegami, H., Ohtsuka, K., Masato, K.: Shape derivative of cost function for singular point: Evaluation by the generalized J integral. *JSIAM Letters* **6**, 29–32 (2014)
7. Azegami, H., Fukumoto, S., Aoyama, T.: Shape optimization of continua using nurbs as basis functions. *Struct. Multidiscipl. Optimiz.* **47**(2), 247–258 (2013)
8. Azegami, H., Solution of shape optimization problem and its application to product design. *Mathematical Analysis of Continuum Mechanics and Industrial Applications, Mathematics for Industry 26*, eds. Itou, H., Kimura, M., Chalupcecký, V., Ohtsuka, K., Tagami, D. and Takada, A., Springer, Singapore, 83–98 (2016)
9. Bacani, J.B., Peichl, G.H.: On the first-order shape derivative of the Kohn-Vogelius cost functional of the Bernoulli problem. *Abstr. Appl. Anal.* **2013**, Article ID 384320, 19pp. (2013)
10. Bacani, J.B., Peichl, G.H.: Solving the exterior Bernoulli problem using the shape derivative approach. in *Mathematics and Computing 2013: Springer Proceedings in Mathematics and Statistics*, Vol. 91, eds. Mohapatra, R., Giri, D., Saxena, P.K., Srivastava, P.D., Springer, New Delhi, 251–269 (2014)
11. Bacchelli, F.: Uniqueness for the determination of unknown boundary and impedance with homogenous Robin condition. *Inverse Probl.* **25**(1):015004, 4pp. (2009)
12. Bayili, G., Sene, A., Niane, M.T.: Control of singularities for the Laplace equation. *An. Univ. Craiova Ser. Mat. Inform.* **40**(2), 226–236 (2013)
13. Ben Abda, A., Jaïem, E., Khalfallah, S., Zine, A.: An energy gap functional: cavity identification in linear elasticity. *J. Inverse Ill-Posed Probl.* **25**(5), 573–595 (2017)
14. Ben Ameer, H., Burger, M., Hackl, B.: Cavity identification in linear elasticity and thermo-elasticity. *Math. Methods Appl. Sci.* **30**(6), 625–647 (2007)
15. Burger, M.: A framework for the construction of level set methods for shape optimization and reconstruction. *Interfaces Free Bound.* **5**, 301–329 (2003)
16. Buttazzo, G., Khon, R.V.: Reinforcement by a thin layer with oscillating thickness. *Appl. Math. Optim.* **16**, 247–261 (1988)
17. Cakoni, F., Kress, R.: Integral equations methods for the inverse obstacle problems with generalized impedance boundary. *Inverse Probl.* **29**(1):015005, 19pp. (2013)
18. Cakoni, F., Kress, R.: Integral equations for inverse problems in corrosion detection from partial Cauchy data boundary. *Inverse Probl. Imaging* **1**(2), 229–245 (2007)
19. Caubet, F., Dambrine, M., Kateb, D.: Shape optimization methods for the inverse obstacle problem with generalized impedance boundary conditions. *Inverse Probl.* **29**(11):115011, 26pp. (2013)
20. Colton, D., Kress, R.: *Inverse Acoustic and Electromagnetic Scattering Theory*, 2nd ed, eds. Marsden J. E. and Sirovich, L. Springer, Berlin (1998).
21. Correa, R., Seeger, A.: Directional derivative of a minimax function. *Nonlinear Anal. Theory Meth. Appl.* **9**, 13–22 (1985)
22. Delfour, M.C., Zolésio, J.-P.: *Shapes and Geometries: Metrics, Analysis, Differential Calculus, and Optimization*, 2nd ed. Adv. Des. Control **22** SIAM, Philadelphia (2011)
23. Doğan, G., Morin, P., Nochetto, R.H., Verani, M.: Discrete gradient flows for shape optimization and applications. *Special Issue Honoring the 80th Birthday of Professor Ivo Babuška. Comput. Method. Appl. M.* **196**(3740), 3898–3914 (2007).
24. Ekeland, I., Temam, R.: *Convex Analysis and Variational Problems*. North-Holland Publishing Co., Amsterdam (1976). Translated from the French, *Studies in Mathematics and its Applications*, Vol. 1.
25. Haslinger, J., Neittaanmäki, P.: *Finite Element Approximation for Optimal shape design: Theory and applications*. John, Wiley & Sons LTD. Chichester. New York. Brisbane. Toronto. Singapore. (1988)
26. Hecht, F.: New development in FreeFem++. *J. Numer. Math.* **20**(3-4), 251–265 (2012)
27. Imam, M.H.: Three dimensional shape optimization. *Int. J. Num. Meth. Engrg.* **18**, 661–673 (1982)
28. Inglese, G.: An inverse problem in corrosion detection. *Inverse Probl.* **13**(4), 977–994 (1997)
29. Inglese, G., Santosa, F.: An inverse problem in corrosion detection. *Pubblicazioni dell’Istituto di Analisi Globale ed Applicazioni del CNR Firenze.* no. 75 (1995)
30. Jaïem, E.: Shape derivative of an energy error functional for voids detection from sub-Cauchy data. *Electron. J. Differential Equations.* **2016**(265), 1–13 (2016)
31. Jaïem, E., Ben Abda, A., Rjaïbi, B.: Cavities identification from partially overdetermined boundary data in linear elasticity. *J. Appl. Computat. Math.* **5**(1), 295, 9p. (2016)
32. Jones, D.A.: *Principles and Prevention of Corrosion*. Prentice Hall, Upper Saddle River, NJ (1996)
33. Karageorghis, A., Lesnic, D., Marin, L.: The method of fundamental solutions for the detection of rigid inclusions and cavities in plane linear elastic bodies. *Comput. Struct.* **106–107**, 176–188 (2012)
34. Karageorghis, A., Lesnic, D., Marin, L.: The method of fundamental solutions for three-dimensional inverse geometric elasticity problems. *Comput. Struct.* **166** 51–59 (2016)

35. Kasumba, H.: Shape optimization approaches to free-surface problems. *Int. J. Numer. Meth. Fluids*. **74**, 818–845 (2014)
36. Kazemzadeh-Parsi, M.J., Daneshmand, F.: Cavity-shape identification with convective boundary conditions using non-boundary fitted meshes. *Numer. Heat Tr. B-Fund.* **57**, 283–305 (2010)
37. Kubo, S.: Inverse analyses and their applications to nondestructive evaluations. in *Proc. 12th A-PCNDT 2006 - Asia-Pacific Conference on NDT*, Auckland, New Zealand (2006)
38. Kurahashi, T., Maruoka, K., Iyama, T.: Numerical shape identification of cavity in three dimensions based on thermal non-destructive testing data. *Eng. Optim.* **49**(3), 434–448 (2017)
39. Meftahi, H., Zolésio, J.-P.: Sensitivity analysis for some inverse problems in linear elasticity via minimax differentiability. *Appl. Math. Model.* **39**(5-6), 1554–1576 (2015)
40. Meftahi, H.: Stability analysis in the inverse Robin transmission problem. *Math. Methods Appl. Sci.* **40**, 2505–2521 (2017)
41. Mendoza, R., Keeling, S.: A two-phase segmentation approach to the impedance tomography problem. *Inverse Probl.* **33**(1):015001, 24pp. (2017)
42. Mghazli, Z.: Regularity of an elliptic problem with mixed Dirichlet-Robin boundary conditions in a polygonal domain. *Calcolo.* **29**(3-4), 241–267 (1993)
43. Neuberger, J.: In *Sobolev Gradients and Differential Equations*, Morel J-M, Teissier B (eds). *Lecture Notes in Mathematics*. Springer, Berlin (2010)
44. Pagani, C.D., Pierotti, D.: Identifiability problems of defects with the Robin condition. *Inverse Probl.* **25**(12):055007, 12pp. (2009)
45. Pironneau, O., Mohammadi, B.: *Applied Shape Optimization in Fluid*. Oxford University Press Inc., New York (2001)
46. Rabago, J.F.T., Bacani, J.B.: Shape optimization approach to the Bernoulli problem: a Lagrangian formulation. *IAENG Int. J. Appl. Math.* **47**(4), 417–424 (2017)
47. Rabago, J.F.T., Bacani, J.B.: Shape optimization approach for solving the Bernoulli problem by tracking the Neumann data: a Lagrangian formulation. *Commun. Pure Appl. Anal.* **17**(6), 2683–2702 (2018)
48. Sokolowski, J., Zolésio, J.-P.: *Introduction to Shape Optimization*. Springer, Berlin (1991)
49. Tajani, C., Abouhabaka, J., Samouh, N.: On the existence of solution for an inverse problem. *TWMS J. App. Eng. Math.* **3**(1), 33–45 (2013)
50. Vogelius, M., Xu, J.M.: A nonlinear elliptic boundary value problem related to corrosion modelling. *Quart. Appl. Math.* **56**, 479–505 (1998)
51. Wigley, N. M.: On a method to subtract off a singularity at a corner for the Dirichlet or Neumann problem. *Math. Comp.* **23**, 395–401 (1968)